Mon. Not. R. Astron. Soc. 000, 000–000 (1994)

Gravitational instability in the strongly nonlinear regime: A study of various approximations

B.S. Sathyaprakash[1], V. Sahni[1], D. Munshi,[1] D. Pogosyan,[2] A. L. Melott[3]
[1] *Inter-University Centre for Astronomy and Astrophysics Post Bag 4, Ganeshkhind, Pune 411 007, India*
[2] *Canadian Institute of Theoretical Astrophysics, University of Toronto, Ontario, Canada*
[3] *Department of Physics and Astronomy, University of Kansas, U.S.A.*

29 August 1994

ABSTRACT

We study the development of gravitational instability in the strongly non-linear regime. For this purpose we use a number of statistical indicators such as filamentary statistics, spectrum of overdense/underdense regions and the void probability function, each of which probes a particular aspect of gravitational clustering. We use these statistical indicators to discriminate between different approximations to gravitational instability which we test against N-body simulations. The approximations which we test are, the truncated Zel'dovich approximation (TZ), the adhesion model (AM), and the frozen flow (FF) and linear potential (LP) approximations. Of these we find that FF and LP break down relatively early, soon after the non-linear length scale exceeds R_* – the mean distance between peaks of the gravitational potential. The reason for this break down is easy to understand, particles in FF are constrained to follow the streamlines of the initial velocity field. Shell crossing is absent in this case and structure gradually freezes as particles begin to collect near minima of the gravitational potential. In LP particles follow the lines of force of the primordial potential, oscillating about its minima at late times when the non-linear length scale $k_{\rm NL}^{-1} \simeq R_*$. Unlike FF and LP the adhesion model (and to some extent TZ) continues to give accurate results even at late times when $k_{\rm NL}^{-1} \geq R_*$. This is because both AM and TZ use the presence of long range modes in the gravitational potential to move particles. Thus as long as the initial potential has sufficient long range power to initiate large scale coherent motions, TZ and AM will remain approximately valid. In relation to AM, TZ suffers from a single major drawback – it underestimates the presence of small clumps. Similarly, it predicts the right mean density in large voids but misses subcondensations within them. The reason for this is clear: The artificial removal of power on scales smaller than $k_{\rm NL}^{-1}$ in the initial potential in TZ, designed to prevent shell crossing, causes a substantial fraction of matter (which would have been clustered in N-body simulations) to lie within low density regions at all epochs. On the other hand, TZ is very fast to implement and more accurately predicts the location of large objects at late times.

Key words: Cosmology : theory – galaxies : formation – large scale structure of Universe – methods : statistical

1 INTRODUCTION

The Universe on large scales exhibits remarkable structural features as demonstrated by the numerous investigations of its statistical properties. It is believed that this structure arose via amplification, through gravitational instability, of primordial fluctuations in the density of matter. The evolution of such fluctuations can be studied using the well known hydrodynamical equations for the gravitating fluid. In the past decade several workers have obtained numerical solutions to these equations which confirm that gravitational instability

can lead to the kind of structure observed in the Universe today.

While numerical N-body simulations are mandatory to approach the precise picture, often our understanding of the dynamical processes that lead to these structures comes from various approximations to the fully nonlinear equations that have been propounded. For instance, Zel'dovich showed that gravitational instability generically leads to the formation of two-dimensional sheets, the so called pancakes, the adhesion model which in some sense can be regarded as an extension of the Zel'dovich approximation, demonstrated that matter moves along pancakes towards filaments (which form at the intersection of two pancakes) and then along filaments towards clumps which form at the junction of two filaments (or three pancakes). Thus the Zel'dovich approximation and the adhesion model showed that gravitational instability leads to the formation of cellular structure described by pancakes, filaments and clumps – a result that has also been independently verified by detailed N-body simulations (Zel'dovich 1970; Melott et al. 1983; Melott & Shandarin 1989; Shandarin & Zel'dovich 1989; Melott, Pellman & Shandarin 1994; Sahni & Coles 1994). In recent years several other approximations to the nonlinear equations governing gravitational instability have been proposed. Such approximation schemes serve a dual purpose: Firstly, they have the potential to provide us with insight regarding the physical processes which led to the formation of structure. Secondly, they are as a rule easier to implement and are often computationally less expensive than full N-body simulations. In order to apply a given approximation effectively we should have a clear understanding of the domain of its validity. It might also so happen that certain statistical properties are reproduced by an approximation to the same level of accuracy as in an N-body simulation although certain other statistical properties may be reproduced to a much lower accuracy. For instance, a given approximation might correctly reproduce the void probability function at a given epoch and yet fail to give the correct multiplicity function for overdense regions. It is therefore essential to examine different non-linear approximations with a number of distinct (and in some cases orthogonal) statistical discriminators.

In the present paper we compare the following approximation methods both with each other and with the results of N-body simulations performed using a two–dimensional PM code running with 512^2 particles on a 512^2 mesh (for details see (Beacom et al. 1991)). We tested: (a) Zel'dovich approximation (truncated version), (b) the adhesion model, (c) frozen flow approximation and (d) linear potential approximation. In a parallel study, we follow the development of gravitational instability using a variety of statistical indicators which probe its different features. The statistical indicators which are used for comparing (a) – (d) single out certain features of non-linear clustering such as the existence of voids, filaments (analogues of pancakes in 2D) and clumps. The domain of validity of a given approximation is therefore discussed with reference to a given statistical indicator.

The treatment followed in this paper extends earlier work of Coles, Melott & Shandarin (1993) in which three nonlinear approximations: the Zel'dovich approximation, the truncated Zel'dovich approximation, and the lognormal approximation were compared with N-body simulations. The present treatment is also in a sense complementary to recent work (Munshi & Starobinsky 1994; Bernardeau et al. 1994; Munshi, Sahni & Starobinsky 1994), in which several of the approximations considered by us were examined in the weakly nonlinear regime of gravitational instability. A common conclusion drawn in the above papers was that the Zel'dovich approximation was more accurate than either the frozen flow or the linear potential approxi-

mation when tested against the results of perturbation theory in the quasi-linear regime. (This analysis was generalised to include Lagrangian perturbation theories in Munshi, Sahni & Starobinsky (1994). The present paper presents a fully nonlinear treatment of the problem thereby considerably extending the quasi-linear analysis of the above authors. Our tests were conducted in two dimensions and complement the three dimensional analysis of Melott et al. (1994) and Melott, Shandarin & Weinberg (1994). Some of our results may however be carried over to three dimensions as well. The exact formulation of the truncated Zel'dovich approximation used here may be found in Melott, Pellman & Shandarin (1994).

The paper is organised as follows. In section II we briefly discuss the various approximations to gravitational instability that we have chosen to compare with N-body simulations. Section III is divided into several subsections each of which deals with a particular statistic. In section IV we summarize the chief results of our investigations.

2 NONLINEAR APPROXIMATIONS

Consider pressureless matter with density $\rho(t, \mathbf{x})$. The dynamics of such a fluid is governed by the expansion of the Universe as also by inhomogeneities in its distribution. The component of the velocity which arises solely due to inhomogeneities in the density field is known as the peculiar velocity $\mathbf{v}(t, \mathbf{x}) = \dot{\mathbf{r}} - H\mathbf{r}$. The combined evolution of the density ρ, peculiar velocity and the peculiar gravitational potential $\varphi(t, \mathbf{x})$ is given by the following well known system of coupled nonlinear equations:

$$\frac{\partial \rho}{\partial t} + 3H\rho + \frac{1}{a}\nabla \cdot (\rho \mathbf{v}) = 0, \tag{1}$$

$$\frac{\partial \mathbf{v}}{\partial t} + \frac{1}{a}(\mathbf{v} \cdot \nabla)\mathbf{v} + H\mathbf{v} = -\frac{1}{a}\nabla\varphi, \tag{2}$$

$$\nabla^2\varphi = 4\pi G a^2(\rho - \rho_0), \tag{3}$$

where $a(t)$ is the cosmic expansion factor, H is the Hubble parameter and ρ_0 is the average density of the fluid. The spatial derivatives in (1) – (3) are defined with respect to the comoving coordinate $\mathbf{x} = \mathbf{r}/a$. Choosing a new time variable $a(t)$, and defining a *comoving* velocity variable

$$\mathbf{u} = \frac{d\mathbf{x}}{da} = \frac{\mathbf{v}}{a\dot{a}}, \tag{4}$$

we obtain the following form for the Euler equation (2):

$$\frac{\partial \mathbf{u}}{\partial a} + (\mathbf{u} \cdot \nabla)\mathbf{u} = -\frac{3}{2a}(\mathbf{u} + A\nabla\varphi), \tag{5}$$

where $A = 2/(3H^2a^3)$ is a constant for a flat Universe with dust-like matter. In cosmological problems, where initial perturbations correspond to the growing scalar mode, the velocity field $\mathbf{u}$ is potential $\mathbf{u} = -\nabla\Phi$ until multistream regions develop.

At earlier moments of time when inhomogeneities are small the solutions to equations (1)-(5) may be obtained by linearization. We then have during the linear stage

$$\mathbf{u}(\mathbf{q}) = -A\nabla\varphi(\mathbf{q}) \tag{6}$$

where $\mathbf{q}$ are the initial (Lagrangian) coordinates. Therefore, initally, the velocity potential and the gravitational potential are simply proportional to one-another $\Phi(\mathbf{q}) = A\varphi(\mathbf{q})$, both unchanging in a flat matter dominated Universe.

Later, in the nonlinear regime, there is no easy solution to the basic system (1)-(5). The different nonlinear approximations considered by us can be conveniently described as different ways of simplifying equation (5).

2.1 Truncated Zel'dovich Approximation (TZ)

The Zel'dovich approximation (henceforth ZA) may be obtained from (5) by setting its right hand side to zero:

$$\frac{D\mathbf{u}}{Da} \equiv \frac{\partial \mathbf{u}}{\partial a} + (\mathbf{u} \cdot \nabla)\mathbf{u} = 0. \tag{7}$$

where D/Da is the convective derivative. The above equation says that the dynamics of the fluid element

is governed purely by "inertia". It has an immediate solution in terms of the displacement of the fluid element from its initial position with constant velocity (Zel'dovich 1970)

$$\mathbf{x} = \mathbf{q} + a(t)\mathbf{u}(\mathbf{q}) \tag{8}$$

By setting the right-hand side of eq.(5) to zero in ZA, one extrapolates the linear relation (6) between velocity and gravitational potential into nonlinear regime where the potentials are generally time dependent $\mathbf{u}(\mathbf{x},t) = -A\nabla\varphi(\mathbf{x},t)$.

ZA works reasonably well so long as streamlines of flows do not cross one another. However, multistream flows invariably form at the locations of pancakes, which grow progressively thicker leading to the ultimate break down of the Zel'dovich approximation (Shandarin & Zel'dovich 1989). An extension of ZA called the truncated Zel'dovich approximation (Coles, Melott & Shandarin 1993) is based on the observation that the formation and thickening of pancakes can be delayed by artificially removing power on all scales smaller than the one that is currently going nonlinear. The length scale and window shape with which the original spectrum is best smoothed has been determined in three dimensions by Melott, Pellman & Shandarin (1994). In our simulations we have used a k-space Gaussian window $\exp(-k^2/2k_G^2)$ to implement the necessary truncation. As found by Melott, Pellman & Shandarin (1994). the optimal cutoff scale is related to the scale entering nonlinearity. However, the precise filtering scale k_G^{-1} depends on the spectrum. This represents a drawback of the model as we cannot obtain the best results for an arbitrary spectrum based on first principles. However, the cutoff scale is only weakly spectrum dependent. The optimal value of k_G^{-1} for spectra considered in this paper will be discussed in the next section (cf. Table II). Nevertheless, let us note that even if we do not use the best filter for a given spectrum but a fixed spectrum independent filtering $k_G \neq k_G(n)$ the approximation still retains most of its positive features. One major advantage of the TZ is the extreme simplicity of its implementation.

An extension of TZ is the use of second order perturbation theory combined with the smoothing of the initial potential. This produces somewhat more accurate but not qualitatively different results from TZ (Buchert, Melott & Weiss 1994; Melott, Buchert, and Weiss 1994). We do not include this second-order approach in this study.

2.2 Adhesion Model (AM)

The adhesion model is an extension of the Zel'dovich approximation. In the adhesion approximation the right hand side of (5) is replaced by an artificial viscosity term to mimic the effects of nonlinear gravity on small scales and to stabilise the thickness of pancakes. The resulting equation is the well known Burger's equation and has the form (Burgers 1974; Gurbatov, Saichev, & Shandarin 1985,1989)

$$\frac{\partial \mathbf{u}}{\partial a} + (\mathbf{u}.\nabla)\mathbf{u} = \nu\nabla^2\mathbf{u}, \tag{9}$$

where ν is the coefficient of viscosity. It is interesting that in the limit $\nu \longrightarrow 0$ the right hand side of (9) remains finite only in those regions where large gradients in the velocity field exist (viz inside the pancakes), and vanishes elsewhere. As a result the adhesion model reproduces the results of the Zel'dovich approximation exactly in regions outside of the pancakes themselves. Accordingly, the adhesion model reduces to ZA for the early time moments or sufficiently smoothed initial conditions when no shell-crossing is present. For vanishing ν the adhesion model has an elegant geometrical interpretation which we have used to construct the skeleton of the large scale structure predicted by this model (Gurbatov, Saichev, & Shandarin 1985,1989; Pogosyan 1989; Kofman, Pogosyan, & Shandarin 1990; Kofman

et al. 1992; Sahni, Sathyaprakash & Shandarin 1994). An undesirable limitation of the geometrical prescription is that it does not give particle positions but only locations of filaments and clumps which have to be smoothed by an appropriate filter in order to lend themselves to a comparative treatment with other models and with N-body simulations. A study using particles (Melott, Shandarin, & Weinberg 1994) in three dimensions shows general agreement with our results when equivalent tests were done.

2.3 Frozen Flow Approximation (FF)

The underlying philosophy of FF is in a sense just the converse of ZA since the inertia of particles is neglected in this approximation which requires particles to constantly upgrade their velocity to a value determined by the local value of the linear velocity field. More precisely, FF corresponds to neglecting both the nonlinear term, namely, $(\mathbf{u}\cdot\nabla)\mathbf{u}$ and the right-hand side in (5) (Matarrese et al. 1992)

$$\frac{\partial \mathbf{u}}{\partial a} = 0 \tag{10}$$

so that the comoving velocity field remains fixed to its linear value $\mathbf{u}(\mathbf{x},t) = \mathbf{u}(\mathbf{q}=\mathbf{x})$. It is clear that matter in FF is collected with time in the points $\mathbf{u}(\mathbf{q}) = 0$ i.e. in the positions of the local minima of the initial gravitational potential. Therefore FF cannot be expected to work even qualitatively for late time moments when the scale of nonlinearity escalates above the typical distance between minima of the initial potential.

2.4 Linear Potential Approximation (LP)

N-body simulations show that the gravitational potential evolves much more slowly than the density field (Brainerd, Scherrer & Villumsen 1993). This is so because relative to δ the potential φ is dominated by small–k modes which obey the precepts of linear theory longer than large–k modes. The linearized Poisson equation $\nabla^2\varphi = 4\pi G a^2 \delta\rho$ demonstrates that $\varphi \simeq$ const. as long as $\delta \ll 1$ and the Universe is flat and matter dominated. Extending this assumption ($\varphi \simeq$ const.) into the nonlinear regime as well, we arrive at the following generalisation of the Euler equation which describes the dynamics of the linear potential (or *frozen* potential) approximation (Brainerd, Scherrer & Villumsen 1993; Bagla & Padmanabhan 1994)

$$\frac{\partial \mathbf{u}}{\partial a} + (\mathbf{u}\cdot\nabla)\mathbf{u} = -\frac{3}{2a}(\mathbf{u} + A\nabla\varphi_0), \tag{11}$$

where $\varphi_0 \equiv \varphi(\mathbf{x},t_0) = \varphi(\mathbf{q})$. This equation defines the force acting on a fluid element at the instant $a(t)$ using the primordial value of the potential $\varphi = \varphi_0$. In a sense the LP can be regarded as an N-body simulation in which the value of the potential is not upgraded after each time step.

Both TZ and AM have single-step analytical solutions. Consequently, there is no need to evolve the fluid iteratively; given some initial conditions these approximations have the ability to directly give the configuration at any epoch which may be of interest. In contrast, LP and FF are Eulerian approximations and have no analytical solutions except in some special cases. Operationally they are similar to full N-body simulations which evolve the fluid iteratively, except for the fact that in LP the potential is kept frozen to its initial value and in FF neither is the velocity potential upgraded nor is particle inertia taken into account. Since PM type N–body simulations are easy to do on modern computers, it is not clear whether LP and FF have value beyond the descriptive insight which they provide.

3 COMPARATIVE STUDY OF VARIOUS APPROXIMATIONS

In this section we employ a number of statistical tools to compare the approximations mentioned in the previous section with N-body simulations. We use the same initial conditions for all the approximations and they

form a subset of the initial conditions used by Beacom et al. (1991) and Kofman et al. (1992) for other purposes. Time evolution of the N–body models can be seen in the video accompanying Kofman et al. (1992). All our comparisons are carried out in two dimensions with the initial potential being specified on a grid of size 512×512. More specifically, the models for which we have carried out the comparison are either featureless or truncated power law spectra of the general form

$$P(k) \propto \begin{cases} k^n, \text{ for } k \leq k_c; \\ 0, \text{ for } k > k_c. \end{cases} \tag{12}$$

We have considered three different spectral indices, $n = 2,\ 0,\ -2$, with a cutoff in each case, at the Nyquist wavenumber: $k_c = 256 k_f$, where k_f is the fundamental mode. In addition to this, we have a $n = 0$ model with a truncation at $k_c = 32 k_f$ which serves to illustrate the effect of an abrupt cutoff in the power spectrum as happens in some models of dark matter like hot dark matter. Thus, we have a total of four models in all.

All our simulations of the various approximations are performed using a particle code excepting the adhesion model which is simulated using the well known geometrical interpretation of the solution to Burger's equation (Shandarin & Zel'dovich 1989; Pogosyan 1989; Sahni, Sathyaprakash & Shandarin 1994). Consequently, we could not include adhesion in studying some statistical properties, such as the position correlation coefficient or filament statistics, which rely on having particle positions. Where we could compare AM with N-body we expect the former to do somewhat better than what our results convey. See also (Melott, Shandarin, & Weinberg 1994) for a particle–based three–dimensional study of AM.

We compare the evolved density fields and the quantities derived from them when different scales are going nonlinear. We choose $\sigma(k_{\rm NL})$, the epoch when the scale $2\pi/k_{\rm NL}$ is going nonlinear, as a convenient measure of "time" with which to characterize different regimes in nonlinear gravitational clustering:

$$\sigma(k_{\rm NL}) = \left(\frac{\int_{k_f}^{k_{\rm N}} P(k) k dk}{\int_{k_f}^{k_{\rm NL}} P(k) k dk} \right)^{1/2}. \tag{13}$$

Here $k_{\rm N}$ is either the Nyquist wavenumber or the cutoff mode k_c, whichever is smaller. For truncated power law spectra (with a cutoff at k_c)

$$\sigma(k_{\rm NL}) = \left(\frac{k_c}{k_{\rm NL}} \right)^{\frac{n+2}{2}}, \quad n \neq -2, \tag{14}$$

and

$$\sigma(k_{\rm NL}) = \left(\frac{\ln (k_c/k_f)}{\ln (k_{\rm NL}/k_f)} \right)^{\frac{1}{2}}, \quad n = -2. \tag{15}$$

The first scale to go nonlinear is the one corresponding to either the Nyquist wavenumber (in the case of models with no cutoff) or the mode k_c. When this happens, by definition, $\sigma = 1$. As σ increases, successively larger scales enter the nonlinear regime. For concreteness we have considered in our comparison those values of σ for which the scales going nonlinear are k_c, $k_c/2$, etc., and we stop the integration when the scale entering the nonlinear regime comes close to the size of the simulation box.

In this study we suggest that two natural scales characterizing a given model may be well suited for giving bounds on the validity of some approximation methods. These are: (i) the scale R_*, corresponding to the average distance between the peaks of the potential and (ii) the scale R_φ characterizing the correlation length of the potential. They are given in terms of the moments of the potential field by the following expressions:

$$R_\varphi = \sqrt{2} \frac{\sigma_0}{\sigma_1} \qquad R_* = \sqrt{2} \frac{\sigma_1}{\sigma_2} \tag{16}$$

where the moments σ_j are defined by

$$\sigma_j^2 \propto \int_{k_f}^{k_c} k^{2j-4} P(k) k dk. \tag{17}$$

The epoch σ_* (σ_φ) when the scale R_* (R_φ) is going nonlinear can be found from (14) and (15) by substituting $k_{\rm NL} = R_*^{-1}$ (R_φ^{-1}). The values of σ_* and σ_φ are listed in Table I for the various models under discussion. The

	$k_c = 32k_f$		$k_c = 256k_f$	
n	σ_*	σ_φ	σ_*	σ_φ
−2	2.36	∞	2.55	∞
0	3.75	20.3	4.71	120
+2	4.00	14.0	4.00	22.2

Table 1. The scales R_* and R_φ of potential corresponding to the average distance between the peaks of the potential and the correlation length, respectively. The box is assumed to be of unit length. Also tabulated are the corresponding epochs σ_* and σ_φ when these scales go nonlinear.

values of R_* and R_φ as well as $\gamma = R_*/R_\varphi$ are plotted in Fig. 1 as functions of the spectral index n.

The values of R_* and R_φ as well as $\gamma = R_*/R_\varphi$ are plotted in Fig. 1 as functions of the spectral index n.

We recognize that the specific values of $\sigma_*(\sigma_\varphi)$ and $R_*(R_\varphi)$ are often (and in particular in our case of power-law initial potentials) determined mainly by numerical cutoffs introduced by the limitations of our computer simulation. In fact this reflects once again the effect of the finite grid used in any simulations on the representation of the underlying initial spectrum. For the real Universe and spectra such as CDM, physical cutoffs are provided by the horizon scale (for R_φ) and by the free-streaming distance (for R_*).

As mentioned earlier in Sec. 2.1 the optimal smoothing scale that needs to be used in TZ simulations depends on the spectrum. By definition, the optimal smoothing scale is that scale which obtains the maximum correlation coefficient of TZ density fields with N-body density fields. We have found that its relation to the scale entering nonlinearity is fairly independent of the epoch. (If this were not so then the very concept of truncated Zel'dovich approximation would lose its meaning.) Table II lists the optimal smoothing scales $k_G^{-1} = k_{\rm opt}^{-1}$ for different spectra considered by us.

3.1 Visual comparison

To begin with, we make a visual comparison of the various approximation schemes with N-body simulations. The structure obtained using the AM and the evolved particle positions in the case of FF, LP and TZ are shown in Fig. 2a-d for four different spectra. From top to bottom, the pictures correspond to N-body, adhesion model, frozen-flow approximation, linear potential approximation, and truncated Zel'dovich approximation, respectively. Fig. 2a corresponds to $n = 0$, $k_c = 32k_f$ model and Fig. 2b to $n = 0$, $k_c = 256k_f$ model. In Fig. 2c and 2d the spectral index is $n = 2$, and -2, respectively, and $k_c = 256k_f$ in both the cases. In Fig. 2a, b and d the left hand panels correspond to an epoch σ such that $\sigma \sim \sigma_*$ ($k_{\rm NL}^{-1} \sim R_*$) and the right panels to an epoch $\sigma \sim \sigma_\varphi$ ($k_{\rm NL}^{-1} \sim R_\varphi$). In Fig. 2c both the left and the right hand panels correspond to an epoch $\sigma > \sigma_\varphi$. (In the case of $n = 2$ models there is a lot of small scale power. Consequently, the pictures at a stage when R_* is going nonlinear looks too grainy. Therefore it is not easy to compare them visually at that epoch.)

We find that at the epoch when the scale going nonlinear is R_*, and at earlier epochs, all the approximation schemes appear to reproduce the structure with roughly the same accuracy as in N-body simulations. (This is also reflected by the high value of the correlation coefficient before the epoch σ_* as discussed in sections 3.2.1 and 3.2.2 – see Fig. 4 and 5).

The epoch corresponding to $k_{\rm NL}^{-1} \simeq R_*$ characterizes the completion of cellular structure which forms from an initially smooth distribution of matter. Later epochs are characterised by the relative motion and mergers of the structure elements governed by mutual attraction of

n	$k_{\rm opt}/k_{\rm NL}$
-2	0.5—1.50
0	1.25
+2	1.00

Table 2. The optimal smoothing scale $k_{\rm opt}^{-1}$ used in the truncated Zel'dovich approximation scheme depends on the index of the power spectrum as shown above. For $n = -2$ spectra the density correlation coefficient is virtually the same for a wide range of values of $k_{\rm opt}$.

large mass concentrations (knots and filaments) as well as repulsion from underdense interiors of cells (voids). It is clear that both FF and LP which fix the structure on scale R_* are unable to describe this process even qualitatively, and therefore begin to fail beyond the epoch σ_*. These conclusions are borne out by Fig. 2a-d.

From the right panels it is clear that close to the epoch when the scale going nonlinear is R_φ the structure obtained using AM is still in excellent visual agreement with that of N-body simulations. TZ has a reasonably good visual agreement with N-body on large scales though at this epoch the small scale features abundant in N-body simulations (especially for spectra with $n \geq 0$) are not present in the TZ simulation. However, much before this epoch, in fact soon after the scale R_* has crossed nonlinearity, FF and LP approximations fail to give the right picture. Particles in FF, approach the valleys and the minima of the potential asymptotically, leading to greatly thinned out filaments which eventually empty out and vanish as the particles gradually fall into the minima of the potential. In the case of LP, particles execute oscillations around the troughs of the primordial potential partially simulating, at earlier epochs, the results of N-body simulations wherein the pancakes neither thicken as in the Zel'dovich approximation nor do they thin out as in FF. The contour diagrams of the initial potentials used in our simulations, shown in Fig. 3, bear out this claim about the behaviour of particles in FF and LP. Notice especially the pictures corresponding to the $n = 2$ power-law model (cf. Fig. 2c) which has a lot of small scale power. Here we see that the particle positions in FF and LP are essentially frozen beyond the epoch $k_{\rm NL}^{-1} \simeq R_*$. While the dynamics in LP and FF at all times are determined by the gradients of the local primordial potential, we know from N-body simulations that beyond the epoch of formation of cellular structure, the small scale features of the primordial potential play little, if any, role in the furtherance of gravitational clustering (Beacom et al. 1991; Pogosyan 1990; Little, Weinberg, Park 1991; Pauls and Melott 1994). It is therefore to be expected that LP and FF will not be able to reproduce qualitatively the features of hierarchical clustering.

The visual agreement of the pictures obtained using AM and TZ with N-body lasts for epochs much longer than that for either FF or LP since the former two approximations successively use power on larger scales to influence the dynamics of the fluid. Even though the local gravitational potential has changed substantially by the time R_* has gone nonlinear, it has not evolved so much as to compete with the effect of power on large scales. Thus, as long as the initial potential has sufficient large scale power to give rise to coherent motion over large scales, TZ and AM will remain approximately valid. Following Kofman et al. (1992) we speculate that the coherence length R_φ of the primordial potential is important in this discussion. By the time σ_φ when the scale R_φ goes nonlinear, in fact even at slightly earlier epochs, both AM and TZ begin to produce structure substantially different in small detail from that seen in N-body simulations. However, it is impossible to determine from our results whether this change is due to a

transition at R_φ or our increasing ability to resolve detail as the simulation goes nonlinear on larger scales. TZ does not produce small objects, and AM puts them in the wrong place. Pauls & Melott (1994) have shown that even at much later times than σ_φ, the primordial potential can determine the coherent motion of large clumps, and TZ can produce correct positions for them while AM begins to make errors in the position of large objects as well and all other approximations have broken down long before. However, let us stress that both TZ and AM continue to reproduce qualitative features of the structure even beyond R_φ.

The TZ approximation suffers from one major drawback. Since in this approximation we have artificially removed power on small scales, matter never gets collected in small clumps. It does, however, put about the right amount of mass in large clumps. Consequently, a substantial fraction of matter (which would be in small clumps in an N–body simulation) lies within low density regions at all epochs. As a result TZ (which has the advantage of being computationally very fast) is not well suited for studying small clumps even though it gives a remarkably good correlation coefficient when compared with N-body simulations. Similarly TZ gives the right mean density in large voids but misses subcondensations within them. This is the price it pays for its greater accuracy in locating the large–scale mass distribution. These views, based largely on a visual comparison of the different approximations, are borne out by more quantitative comparisons which we discuss below. The AM suffers from two major drawbacks. First, it is computationally expensive, sometimes approaching the cost of an N–body simulation. Second, although it does produce small clumps, it occasionally makes major errors in their position (sometimes comparable with the scale of nonlinearity), especially at late times and larger n.

3.2 Quantitative comparison

We now turn to a quantitative comparison of the various approximation schemes with N-body simulations. The information about any statistic can in principle be inferred from a knowledge of all the N-point correlations, or at least a substantial number of them. In practice, however, the full hierarchy of correlation functions is virtually impossible to calculate due to heavy computing requirements. Even if it were in principle possible to compute the higher order correlation functions it is not clear how much light that would shed on structural units that are often of interest such as clumps and filaments. It is with the aim of studying such structural units that we have chosen a number of statistical tools each of which addresses a specific structural feature present in the simulation. To this end we choose the time evolution of the following indicators for comparison:

(i) Correlation coefficient of particle positions of different approximation schemes with N-body,

(ii) Correlation coefficient of density fields of different approximation schemes with N-body,

(iii) Number of *clumps,* (defined as regions of a certain overdensity),

(iv) *Filament* statistics,

(v) Number of *voids,* (defined as regions of a certain underdensity),

and

(vi) *Void probability function.*

We note that the first two indicators are primarily dynamical, in that they test for specific point–by–point agreement between the approximation and the N–body simulation. The others are global statistics, and test for particular kinds of similarity.

3.2.1 Correlation coefficient of particle positions

Given an approximation scheme an obvious question that comes to mind is how well can the approximation

scheme evolve the particles in relation to the exact N-body simulations. To answer this question we consider the correlation coefficient of the coordinate positions of an approximation scheme and N-body. Let $\mathbf{X}^i_{\rm A}(\sigma)$ and $\mathbf{X}^i_{\rm N}(\sigma)$ denote the position of the i th particle, at an epoch $\sigma(t)$, in an approximation A and N-body, respectively. The displacement of the particles from their unperturbed coordinates $\mathbf{X}(\sigma(t_0))$ is given by:

$$\Delta\mathbf{X}(\sigma(t)) = \mathbf{X}(\sigma(t)) - \mathbf{X}(\sigma(t_0)) \tag{18}$$

The linear correlation coefficient of two vector fields $\Delta\mathbf{X}_{\rm A}(\sigma(t))$ and $\Delta\mathbf{X}_{\rm N}(\sigma(t))$ is defined by

$$r_{\mathbf{X}} \equiv \frac{\sum_i \delta\mathbf{X}^i_{\rm A} \cdot \delta\mathbf{X}^i_{\rm N}}{\left[\sum_j (\delta\mathbf{X}^j_{\rm A})^2 \sum_k (\delta\mathbf{X}^k_{\rm N})^2\right]^{1/2}} \tag{19}$$

where a dot denotes the scalar product of the two vector fields, where $\delta\mathbf{X} \equiv \Delta\mathbf{X} - \langle\Delta\mathbf{X}\rangle$ is the deviation of the displacement vector from average displacement, where a summation is over the entire sample and where $\langle\ \rangle$ indicates average over the entire sample. This is a straightforward generalization of the familiar correlation coefficient defined for scalar fields. In Fig. 4 we have plotted the evolution of $r_{\mathbf{X}}$ for different approximation schemes, and for different spectra, as a function of $\sigma(t)$. Here, and in Fig. 4 and 10, we adopt the following scheme for displaying the evolution of different statistics: The top left panel corresponds to $n = 0$, $k_c = 32k_f$ model and the top right panel to $n = 0$, $k_c = 256k_f$ model. The bottom left panel corresponds to $n = 2$ model and the bottom right panel to $n = -2$. In Fig. 4 the results AM are missing since our implementation of this approximation scheme (using an osculating paraboloid) does not obtain particle positions.

We observe that when the spectral index $n = -2$ there is an excellent agreement between all the three approximations and the N-body. ($r_{\Delta\mathbf{X}}$ is always larger than about 0.9 for all approximations for this spectrum.) In the $n = 2$ case, surprisingly, the correlation vanishes to begin with, building up later to reach a maximum of about 0.6 before dropping. We do not understand this behaviour entirely but suspect that some numerical effect from the excessively large power on very small scales present in this case is the root cause for such a behaviour. In this case we see that none of the approximations produce the right kind of displacement of particles. This is absolutely in agreement with Fig. 2c (corresponding to $n = 2$ spectrum) wherein we see that in the case of both FF and LP matter simply gets collected into the local minima of the potential without ever transferring the power to larger scales while in the case of TZ matter does not cluster on small scales at all. Although the agreement of all approximations with N-body is relatively poor for this spectrum, we find that TZ gives consistently higher values for the correlation coefficient especially at late times when clustering is more prominent on large scales.

From Fig. 4 we find that for spectra with substantial power on a wide range of scale, such as $n = 0$ or $n = 2$, particle positions in TZ agree with those in N-body much better than do either LP or FF. This is because of the fact that for such spectra, wherein both small and large scales dictate the dynamics (with larger scales being more important at later epochs) LP and FF break down at relatively earlier epochs than TZ and AM.

3.2.2 Correlation coefficient of density fields

While the correlation coefficient of particle positions tells us precisely how the structure is produced in an approximation scheme it is seldom the main quantity of interest; it is only a measure of how good a dynamical approximation scheme is in relation to the N-body solutions. One is often interested in the evolution of the density field since it lets us infer the evolution of many other structural units such as clumps, filaments and voids. In order to study the time evolution of the density field we obtain the density field by employing the cloud-in-cell (CIC) algorithm. This algorithm can

only be used when particle positions are known and hence cannot be directly used for our AM simulations. In the latter case, we use the structural units of clumps and filaments (plus the "free" particles – those that have not yet fallen into caustics) given by the model to reconstruct the density field. The density field for AM simulations is obtained in three steps: (i) The mass in the "free" particles is distributed using the CIC algorithm. (ii) Each clump given by AM is assumed to be a "Gaussian hill" with the variance of the Gaussian chosen to be proportional to its mass. (iii) The rest of the mass is distributed uniformly amongst filaments which is then smeared using the CIC algorithm.

The density fields so obtained are smoothed at a certain scale before computing the correlation coefficient. Such a smoothing is motivated by the fact that the density fields evolved by approximation schemes are not expected to agree with those of N-body simulations in great detail; any agreement is to be expected only after the small scale inhomogeneities are smoothed out. In fact, the relevant question here is: "How well can a given approximation mimic the results of exact equations on medium scales?". The physical reason for this is that the very large scale properties of the universe can be studied by ZA or Eulerian perturbation theory, while the smallest ones by N–body simulations plus hydrodynamics. We might mention that an improvement in the correlation coefficient for TZ is expected if instead of filtering the density on a fixed scale, say, $k \simeq 64 k_f$, a variable filter scale which is a constant multiple of the scale of non-linearity $k \propto k_{\rm NL}$ is chosen. This is demonstrated in Fig.5b for a density which is filtered on a scale $k = 2k_{\rm NL}$ for the spectrum $n = 0$, $k_c = 256 k_f$.

Following Coles Melott & Shandarin (1993) we use the correlation coefficient of density fields to compare the approximation schemes with N-body simulations. Given density fields $\rho_{\rm A}(\sigma)$ and $\rho_{\rm N}(\sigma)$, corresponding to an approximation scheme A and the N-body simulation, respectively, the correlation coefficient of these fields is defined by a formula similar to equation (19):

$$r_\delta \equiv \frac{\sum_i \delta^i_{\rm A} \delta^i_{\rm N}}{\left[\sum_j (\delta^j_{\rm A})^2 \sum_k (\delta^k_{\rm N})^2\right]^{1/2}} \qquad (20)$$

where $\delta \equiv (\rho - \rho_0)/\rho_0$ is the density contrast.

The evolution of the statistic r_δ is shown in Fig. 5a. The arrangement of the panels here is as in Fig. 4. Here we have also included the results of the adhesion model. We notice that except for the $n = 2$ model TZ and AM are in better agreement with N-body than FF and LP. For the $n = 2$ model AM, FF and LP, all give roughly the same correlation at all epochs, while TZ is better. In contrast to the pictures wherein the agreement of TZ with N-body is not so remarkable, the density correlation is extremely good up to very late times. In absolute terms however, both TZ and AM eventually break down. The results of AM shown here are entirely consistent with those found before (Melott, Shandarin, & Weinberg 1994) using a particle AM code, in spite of the artificial smoothing of filaments and clumps that has gone into our code to make the geometrical method mimic the particle method. In the case of $n = 0$ power-law models, we note that soon after the epoch σ_*, say $\sigma = 8$, while the LP has managed to produce a correlation coefficient of about 0.5, the FF has a far less value at this epoch. However, both the AM and the TZ give values substantially larger than 0.5 indicating their validity at this and later epochs. The reason why the FF does so badly can be traced to Fig. 2a-d wherein we see that matter has completely emptied out into rivulets of the potential wells by the epoch σ_*.

The superior performance of TZ on scales down to $k_{\rm NL}^{-1}$ combined with its speed makes it a good approximation for studying the mass distribution from scales of about $b^{-1}(1+z)^{-1}10^{13} M_\odot$ on up, where b is the bias parameter and z is the redshift. As we shall see, it fails on smaller scales. But the mass resolution is two orders of magnitude better than in the past.

A good density correlation of an approximation scheme with an N-body simulation does not necessarily mean that other statistical indicators too will give good results when testing the approximation with N-body (unless of course the density correlation approaches unity). Conversely, a poor density correlation does not necessarily imply that the approximation will also predict incorrect results for other statistics. However, our two previous statistics, the position and density correlations do test the dynamical accuracy of our approximations. The tests which follow probe agreement with respect to global statistical measures, which is a somewhat different issue. Correct global statistics do not necessarily imply correct dynamics. In what follows, therefore, we supplement the two correlation coefficients discussed above with other statistical indicators that address issues relating to the ensemble of structural units present in the simulation. They do not test whether specific individual units are in same the same place but they do test an overall "resemblance."

3.2.3 Evolution of the number of clumps

An important statistic which any theory of LSS is expected to explain is the mass function of galaxies or of clusters of galaxies: how the total mass is distributed in objects of different masses. A related question is how the number of clumps, defined as connected regions of a certain overdensity, evolves with time. Due to lack of space, here we address only the latter, relegating the more important former question to a future work. The number of clumps, at any moment, clearly depends on the density threshold ρ_c we use to identify regions of overdensity. However, since the aim here is to compare the predictions of different approximations with N-body, it hardly matters what density threshold we choose provided it suffices to obtain well defined clumps. In Fig. 6 we have shown regions in our N-body simulations of density $\rho \geq \rho_c$ at two different epochs each, for the models $n = 0$, $k_c = 32k_f$, and $n = 0$, $k_c = 256k_f$. We see that the clumps are well defined for the chosen density threshold and we use appropriate density thresholds for the different spectra considered by us. A clump is now defined as a connected region, in the sense of a "friends-of-friends" algorithm, of overdensity greater than or equal to the density threshold ρ_c.

In Fig. 7 we have shown the evolution of the number of clumps for different simulations of the various power-law models discussed earlier. The top panels show the evolution of the number of clumps and the bottom panels show the evolution of the fraction of mass in clumps. In Fig. 7a left panels correspond to $n = 0$, $k_c = 32k_f$ model and the right panels to $n = 0$, $k_c = 256k_f$ model. In Fig. 7b the left panels correspond to $n = 2$, and the right panels to $n = -2$, models, respectively. The results of N-body are shown in thick solid lines. Following the N-body curve we see that generically, there are two distinct phases in the clustering of matter via gravitational instability. During the first phase the number of clumps keeps increasing reaching a maximum after the epoch σ_* at which time the formation of cellular structure is complete. By this epoch nearly 50 % of the matter that ever gets bound has fallen into the local wells of the initial potential causing major changes in the local value of the potential without, however, disrupting large scale modes. During the second phase clustering proceeds hierarchically, with smaller clumps merging with one another to form clumps of larger mass. As a result the density contrast of the clumps alone (not shown) keeps building up at a phenomenal rate whereas the number of clumps begins to fall. Roughly, σ_* characterizes the epoch of the transition from the cellular to the hierarchical phase of clustering (Sahni, Sathyaprakash & Shandarin 1994). The gravitational potential on small scales undergoes substantial changes during the second phase culminating in the disruption of any initial small–scale coherence that might have existed in the primordial po-

tential. Further discussion of the evolution of the potential can be found in Pauls & Melott (1994). Beyond the epoch σ_* no approximation scheme which proposes to keep the local values of the potential unchanged, and at the same time does not use large scale power in describing the dynamics, can predict correct gravitational clustering.

Strictly speaking, as far the evolution of clumps is concerned the agreement between N-body simulations and approximation schemes, depends on the spectral index. However, based on Fig. 7 we first make the following general remarks. We note that with the exception of AM none of the other approximations reproduce the expected fall in the number of clumps at late times caused by merger of clumps. In FF and LP the number of clumps, at earlier epochs, show the general trend of a sharp rise and closely resemble the predictions of N-body simulations till about σ_*. However, neither of these approximations show a proper fall off in the number of clumps. In fact, with the exception of the $n = 0$, $k_c = 32k_f$ model, there is no fall off seen in the number of clumps in these approximations which is a major feature of gravitational clustering: In these approximations there is relatively little evolution in the number of clumps at later times. This is in contrast to N-body simulations wherein the merger of clumps, with smaller clumps falling into the wells created by the larger ones, is a never–ending process. The bottom panels of Fig. 7 lend further support to the viewpoint that these two approximations do not predict the correct clustering of matter beyond the epoch σ_*. We observe that in N-body simulations matter gets continuously drained into clumps whereas in none of the approximation schemes, except in AM, is this phenomenon seen generically. We note that the statistics of clumps produced by TZ is almost never in agreement with N-body simulations. The reason for this is that in this approximation the clumps are at no time well defined objects. Clumps are relatively short scale features which form soon after the rms linear density contrast reaches unity. Thereafter they mature, and gain identity by the epoch when the scale going nonlinear is R_*. However, in the case of TZ the linear theory *rms* density contrast is never allowed to greatly exceed unity: power on successively larger scales, in fact power on roughly the scale that is entering nonlinearity, is filtered out. Consequently, although voids are well defined in this approximation, clumps never acquire a permanent identity. The bottom panels of Fig. 7a show that hardly 50 % of the total mass ever gets collected in clumps in TZ. This, in addition to the very low number of clumps that the approximation predicts, makes the approximation scheme unsuitable for any study concerning small scale features of LSS such as individual galaxies. This is a shortcoming of this approximation, but one that is not entirely unexpected.

In our opinion the AM is best suited in describing clustering which statistically resembles N-body simulations. It predicts the right kind of growth law for the fraction of matter in clumps as well as the right merger histories of collapsed objects (except perhaps in the $n = -2$ case).

3.2.4 Filamentary statistics

The second in our study of the structural units of LSS is filaments. In order to understand the formation and evolution of filaments we employ a statistic first suggested by Vishniac (1979) and later used by Nusser and Dekel (1990) to study filamentarity in different models of structure formation. This statistic is obtained by first identifying the moments of the distribution of particles around a chosen centre and then constructing a scalar from these moments.

Let $M_k^{\alpha}(R)$ and $M_k^{\alpha\beta}(R)$ denote the first and second "moments" of the distribution of the particles located within a distance R around the k th particle:

$$M_k^\alpha = \frac{1}{N_k}\sum_{j=1}^{N_k} x_j^\alpha, \tag{21}$$

$$M_k^{\alpha\beta} = \frac{1}{N_k}\sum_{j=1}^{N_k} x_j^\alpha x_j^\beta. \tag{22}$$

Here N_k is the number of particles within a distance R from a centre located at the k th particle, and x_j^α, $\alpha = 1, 2$, denotes the position vector of the j th particle relative to the k th particle. The filamentary statistic $S(R)$ is the ensemble average of the scalar $S_k(R)$ constructed for the chosen center out of the two moments given above:

$$S_k(R) = \frac{2\sum_{\alpha,\beta} M_k^{\alpha\beta} I_k^{\alpha\beta} - \sum_\alpha M_k^{\alpha\alpha}\sum_\beta I_k^{\beta\beta}}{\left(\sum_\gamma M_k^{\gamma\gamma}\right)^2}, \tag{23}$$

where

$$I^{\alpha\beta} = M_k^{\alpha\beta} - M_k^\alpha M_k^\beta \tag{24}$$

and

$$S(R) = \frac{1}{N}\sum_{k=1}^{N} S_k(R) \tag{25}$$

where N denotes the number of centers chosen in carrying over the average. The scalar $S_k(R)$ takes on values in the range $[0, 1]$ attaining its maximum value of unity when the particles are aligned along a straight line passing through the center and zero for a uniform distribution of particles around the centre.

Evidently, using the above statistic we cannot infer about filamentarity given only a density field since we must have information about particle positions in order to compute $S(R)$. Consequently, we will not be able to evaluate this statistic for the adhesion model. (It would certainly be worthwhile to construct a statistic that would work for densities.) For the rest of the approximations and N-body we have chosen, at each epoch, a random sample of about 2% of all the particle positions as "test" centers in computing $S(R)$. The behaviour of $S(R)$ for N-body, FF, LP and TZ simulations is shown in Fig. 8 for two different epochs as indicated by the value of σ quoted within the panels. The two epochs chosen are exactly as in Fig. 2 (see the caption of Fig. 2). The scale R essentially characterizes the length, in grid units, of the filaments being explored.

The N-body curves (thick solid lines) in Fig. 8 show a clear transfer of power from smaller to larger filaments as successively larger scales go nonlinear. This behaviour, reflected by the evolution of the filamentary statistic, is consistent with the visual impression rendered by Fig. 2a-d. For instance, the N-body panels on the left in Fig. 2a, which correspond to earlier epochs, show predominantly small scale filamentarity while those on the right, which correspond to later epochs, show relatively large scale filamentarity. On comparing the value of the statistic for different spectra but at an epoch when the same scale is going nonlinear in all of them we see that S is larger for spectra with lower value of n. Moreover, at later epochs there are in general two preferred scales at which the filaments occur predominantly. This is seen very clearly in the $n = -2$ model (Fig. 8b, bottom panels) wherein we see a lot of power on very small scales, which sharply drops close to zero on intermediate scales but rises again showing substantial filamentarity on large scales. In short, the statistic generically shows, at late times, two prominent peaks (see right panels of Fig. 8a and 8b). This is entirely consistent with what is expected from Fig. 2a-d. This demonstrates that the statistic S truly characterizes filamentarity. (One might want to increase the effectiveness of this statistic by first using an algorithm such as the Minimal Spanning Tree to delineate the main features of the distribution, and then apply the filamentary statistic exclusively to these features (Pearson & Coles 1994; Sahni & Coles 1994).)

At earlier epochs both FF and LP predict the right value of the statistic on most scales and for all spectra. In the case of $n = -2$ models there is an excellent agreement, at all times, between FF, LP and N-body simulations. However, at later epochs none of the ap-

proximations produce the right behaviour of the statistic: FF predicts more power on smaller scales and lesser power on larger scales while LP predicts lower power on almost all scales. The reason why FF produces more power on smaller scales can be seen from panels corresponding to FF in Fig. 2a-d: FF simulations show a lot of filamentarity on small scales and none on large scales. Due to an inherent assumption of this approximation there cannot be any shell crossing. This means that particles approach the "valleys" of the potential with ever decreasing speeds leading to many whisker shaped objects. Matter that gets collected along the streamlines of the velocity field in this way eventually drains out into the minima of the potential wells. As a result, large scale filaments never mature in this approximation. The problem with FF is just the opposite to that with the Zel'dovich approximation: In the latter the pancakes do not remain thin and in the former the pancakes never thicken. Both these aspects are contrary to the findings of N-body simulations. In fact, the fundamental reason why LP and FF cannot produce large scale filaments is because they never use power on large scales and hence cannot build up matter coherently on such scales.

TZ predicts a much lower value of the statistic on all scales and at all epochs. One may think this contrary to what the figures 2a-d seem to indicate, especially on very large scales. However, we recall that in TZ simulations the amount of matter in overdense regions is under 30% at most times (cf. Fig. 7) indicating that a bulk of the matter is distributed diffusely in underdense regions. This means that the strong visual signal that we see (especially in Fig.2c) is not picked up by this statistical test. Consequently, we obtain, in this case, a very low value of S. (One might anticipate a better agreement between TZ and N-body if the low signal-to-noise ratio in TZ were amplified using the Minimal Spanning Tree or a fixed overdensity threshold on which to test for filamentarity.)

3.2.5 Evolution of voids

The next in our list of structural units are voids. There is now a consensus on the view that most of the universe is filled with voids of different shapes and sizes, with most of the matter residing on boundaries separating them. The distribution of volume amongst voids of various sizes, sometimes called the "void spectrum", is quite sensitive to the primordial spectrum of density fluctuations (Kauffmann & Melott 1992; Sahni, Sathyaprakash & Shandarin 1994). Hence a proper understanding of the distribution of voids in the Universe could in principle lead to a precise estimation of the primordial spectrum. Further, Sahni, Sathyaprakash and Shandarin 1994, have pointed out that the void spectrum can potentially be used to determine the value of the density parameter Ω if the shape and amplitude of the initial perturbation spectrum are independently known. Thus, the statistics of voids is an important measure in characterizing the large scale structure of the Universe. In our study of voids we employ two indicators of void statistics: (i) The total number of voids in our simulations (which is a function of epoch), and (ii) the void probability function. The former will be discussed here and the latter in the next subsection.

We define individual voids as connected regions of a given underdensity. As in the case of clumps the number of voids is sensitive to the threshold density chosen for identifying them. Again, since the aim here is to compare the various approximation schemes with N-body, we need only choose an appropriate threshold density so that voids are (visually) well defined. We found that in order to obtain a good picture of voids it is necessary to smoothen the density field before applying the density threshold in selecting void regions. If the density field were not smoothed then there would be too many tiny

voids which would give rise to a lot of "noise" in the evolution of the number of voids without at the same time making any significant contribution to the total volume occupied by voids. In Fig. 9 we have shown regions in our N-body simulations of density $\rho \leq \rho_c$ at two different epochs each for the $n = 0$, $k_c = 32k_f$ model (top panels) and $n = 0$, $k_c = 256k_f$ model (bottom panels). The density fields were smoothed by removing power on modes $k \geq 64k_f$. We see that voids are well defined for the chosen underdensity except that there are still a few voids of very small size. Thus, in our definition of voids we do not take into account voids whose diameters are smaller than 10 grid units.

The evolution of the number of voids plotted in Fig. 10 exhibits behaviour similar to the evolution of clumps seen in Fig. 7: With reference to the N-body curve (thick solid line) we observe that initially there is a sharp increase in the number of voids, it acquires a maximum sometime after the epoch σ_* (except in the $n = -2$ model where there is no peak), and thereafter falls steadily, more or less stabilizing after a while. The voids are not well defined at very early epochs ($\sigma \leq 1$) but by the epoch σ_* they gain their identity. The decline in the number of voids in Fig. 10 is a consequence of the fact that voids compete for space during expansion, and that smaller voids can be encroached upon by larger ones. Thus, voids not only expand they can also contract and ultimately disappear (Sahni, Sathyaprakash & Shandarin 1994).

The adhesion model produces roughly the right evolution for the number of voids, the largest disagreement being for the $n = 0$, $k_c = 256k_f$ model. In the latter case it predicts a slightly smaller number of voids than what is predicted by N-body simulations. FF and LP fail to reproduce the correct evolution of the number voids in all but the $n = 0$, $k_c = 256k_f$ model where they agree with N-body very well. In the case of FF as matter falls into deeper wells of the potential, the cellular structure gets completely phased out with the result that at later epochs very few voids are left behind in this case. In other words, in FF there is no cellular structure to "support" the voids. The same is true in the case of LP but because of the fact that the particles do cross over caustic regions the cellular structure lasts a little longer and the fall off in the number of voids is somewhat slower than in the case of FF. Note especially that in the $n = 2$ model both FF and LP predict only one void at all epochs. This is consistent with the visual pictures corresponding to these approximations (cf. Fig. 2c) which indicate that these simulations will only have one void with a sponge like topology. TZ, as expected from the pictures in Fig. 2, always predicts fewer but larger voids as compared to N-body. This is because regions that are populated by many small clumps in N–body are filled with a low rather uniform density in TZ. It is therefore not a suitable tool to study the void spectrum.

Summarising, the adhesion model is best suited for studying the statistics of voids: It not only predicts the right evolution for the number of voids (the sharp rise and the subsequent gradual fall-off), it also predicts the right number of voids for most spectra at virtually all times.

3.2.6 Void probability function

At late times voids are large scale coherent features and it is hard to draw a definite demarcation boundary about a void. There is great danger in using the "friends-of-friends" algorithm to identify voids, especially at late times. A closer look at Fig. 9 shows that a tiny bridge connecting two neighbouring voids will cause the algorithm to declare as one void what visually would appear to be two distinct voids. For such epochs the void probability function (henceforth referred to as VPF) is a better indicator of the sizes of voids than void number. We therefore supplement the information

obtained by studying the evolution of the number of voids with that obtained using the VPF. The VPF describes the probability that a sphere of size R (a circle in 2D) thrown at random is completely devoid of matter (White 1979). In practice one can relax this condition a little and say that the VPF is the probability of finding that a sphere of radius R placed at random within the simulation box is an "underdense" region. Here again we are faced with a non-objective definition since the results will depend upon the chosen value of underdensity. However, for our purposes of comparison, it makes sense to choose any reasonable underdensity that would be consistent with what the pictures project. We first make a map of the overdense regions as in, say, Fig. 6 and for this map we compute the VPF. We have chosen at random 20 % of all the grid points in computing the VPF.

Our results are shown in Fig. 11a and b (two epochs each) for all the models considered by us. The epochs chosen are the same as in Fig. 8. We notice that the VPF at earlier epochs falls off sharply with scale indicating a scarcity of large voids. At later epochs however, the fall off is slower, indicating the formation of larger voids as the Universe expands. TZ predicts, as expected, a lot more voids on all scales and at all epochs as compared to N-body. The reason for this is simple: At any epoch σ all the power in the primordial potential below the scale $k_{\rm NL}(\sigma)^{-1}$ has been removed in evolving the particles up to the epoch σ and hence one cannot expect the formation of structure on this and lower scales in TZ simulations. In the $n = 0$ models, at earlier epochs AM, FF and LP, all agree with N-body. However, at later epochs the latter two approximations predict fewer voids of all sizes. The reason for this is that matter does not participate in hierarchical clustering in FF and LP and thus matter does not get emptied out as happens in the case of N-body. AM comes closest to the predictions of N-body for this spectrum.

While this is the story in the case of spectra with equal power on all scales the results are totally different when the power is not equal on all scales. In the case of the $n = 2$ model none of the approximations agree with N-body with AM and TZ being closest in accuracy. For $n = -2$ on the other hand FF and LP agree remarkably well with the predictions of N-body both at earlier and later epochs and on almost all scales.

4 CONCLUSIONS

In this work we have studied gravitational instability in the strongly non-linear regime using a number of distinct and sometimes orthogonal statistical indicators such as: Correlation coefficient of particle positions/densities; statistics of overdense and underdense regions (clumps and voids); filamentary statistics; and the Void probability function. Using these statistics we assess the accuracy of different approximations to gravitational instability such as: the Truncated Zel'dovich approximation (TZ), the adhesion model (AM), the frozen flow (FF) and the linear potential (LP) approximation. We compare these approximations with N-body simulations for a variety of spectra and at different cosmological epochs. We find that as the scale of non-linearity grows, so do the characteristic features of structure such as filamentarity and the sizes of voids. Our study shows that as long as the non-linear length scale $k_{\rm NL}^{-1}$ remains smaller than R_* – the typical distance between peaks of the gravitational potential – all approximations give results in reasonable agreement with those of N-body simulations. During the epoch $R_* < k_{\rm NL}^{-1} < R_\varphi$ (R_φ being the correlation length of the potential) the adhesion model (and occasionally TZ) gives results closest to N-body. The reason for this is the following: Particles in FF follow the streamlines of the initial velocity field, converging in the minima of the gravitational potential. As a result, filaments in this approximation, show a tendency to thin out and

ultimately disappear. In the case of LP, particles begin to oscillate about the minima of the potential at late times, freezing the possibility of any long range dynamics. Consequently, no real evolution of particle positions can take place beyond the epoch $k_{\rm NL}^{-1} \simeq R_*$ in either FF or LP which break down when $k_{\rm NL}^{-1} > R_*$.

Unlike FF and LP both AM and TZ use the presence of long range modes in the gravitational potential to move particles at late times. Consequently, as long as the potential has sufficient long range power to affect bulk motion over large scales (described by R_φ), TZ and AM give results closely matching with those of N-body. Compared with AM, TZ suffers from one major drawback: although it does manage to collect the right amount of matter into large clumps it completely overlooks the presence of small clumps. The reason for this is clear, in order to prevent shell crossing all modes which have gone non-linear by a given epoch are surgically removed from the initial gravitational potential because of which no small scale clustering is present in TZ. The adhesion model does not suffer from this drawback and can accurately predict the multiplicity function of clumps and the void spectrum as long as $k_{\rm NL}^{-1} \leq R_\varphi$. However, after $k_{\rm NL}^{-1} \geq R_\varphi$, TZ makes much more accurate predictions about the location of mass. In this regime, AM continues to make better statistical predictions, but its dynamical accuracy is reduced. This can be understood as inaccurate influence of the short modes on the position of structure in AM at late times especially since by construction, the adhesion technique when applied to truncated initial spectrum closely reproduces TZ.

A comparison of R_* and R_φ for different spectra (Fig. 1), shows that $R_* \simeq R_\varphi$ for very steep or very shallow spectra with $n > 2$ or $n < -2$. For intermediate values $-2 \leq n \leq 2$ $R_\varphi \gg R_*$ indicating that for such spectra the adhesion model (and occasionally TZ) will be more accurate than FF or LP. These values of the two dimensional spectral index correspond in three dimensions to the range $-3 \leq n \leq 1$ which is precisely the range of interest in most cosmological scenario's such as CDM. (For the standard CDM model, $R_* < 1$ Mpc. $R_\varphi \simeq 50$ Mpc.) We therefore feel that the adhesion model and the truncated Zel'dovich approximation (depending on which aspect of the description of structure one wishes to emphasize) are more realistic approximations to apply to the study of large scale structure than either FF or LP.

Acknowledgments: ALM wishes to thank the following (all in the USA) for support: The National Center for Supercomputing Applications at Urbana, Illinois, NASA (grant NAGW–3832), and NSF (grant AST–9021414). ALM, DP and VS are grateful to the Aspen (Colorado, USA) Center for Physics for sponsoring a 1994 workshop on this and related topics where this work was completed.

REFERENCES

Bagla, J.S., & Padmanabhan, T., 1994. MNRAS, 266, 227
Beacom, J.F., Dominik, K.G., Melott, A.L., Perkins, S.P., & Shandarin, S.F., 1991, ApJ, 372, 351
Bernardeau, F., Singh, T.P., Banerjee B., & Chitre S.M., 1994, MNRAS, in press
Brainerd, T.G., Scherrer, R.J., & Villumsen, J.V., 1993. ApJ, 418, 570
Buchert, T., Melott, A.L. & Weiss, A.G., 1994, A&A, in press
Burgers, J. M., 1974, The Nonlinear Diffusion Equation (Dordrecht: Reidel)
Coles, P, Melott, A.L., & Shandarin, S.F., 1993, MNRAS, 260, 765
Gurbatov, S. N., Saichev, A. I., & Shandarin, S. F., 1985, Soviet Phys. Dokl. 30, 921
Gurbatov, S. N., Saichev, A. I., & Shandarin, S. F., 1989, MNRAS, 236, 385
Kauffmann G., & Melott, A. L., 1992, ApJ393, 415
Kofman, L. A., Pogosyan, D. Yu., & Shandarin, S. F., 1990, MNRAS, 242, 200
Kofman, L. A., Pogosyan, D. Yu., Shandarin, S. F., & Melott, A. L., 1992, ApJ, 393, 437
Matarrese, S., Lucchin, F., Moscardini, L., & Saez, D., 1992, MNRAS, 259, 437
Melott, A.L., Einasto, J., Saar, E., Suisalu, I., Klypin, A. A., &Shandarin, S. F., 1983, Phys. Rev. Lett. 51, 935
Melott, A.L., Buchert, T. & Weiss, A.G., 1994, A&A, in press
Melott, A.L., Lucchin, F., Matarrese, S., & Moscardini, L., 1994, MNRAS, 268, 69
Melott, A.L., Pellman, T.F. & Shandarin, S.F., 1994, MNRAS, 269, 626
Melott, A. L., & Shandarin, S. F., 1989, ApJ, 343, 26

Melott, A.L., Shandarin, S.F., & Weinberg, D.H., 1994, ApJ428, 28
Munshi, D., & Starobinsky, A.A., 1994, ApJ, 428, 433
Munshi, D., Sahni, V. & Starobinsky, A.A., 1994, ApJ, in press
Nusser, A. and Dekel, A., 1990, ApJ, 362, 14.
Pauls, J. & Melott, A.L., 1994, MNRAS, submitted.
Pearson, R.C. & Coles, P., 1994, MNRAS, submitted
Pogosyan, D.Yu., 1989, Tartu preprint, Estonian Acad. Sci
Pogosyan, D.Yu., 1990, PhD Thesis, Tartu, Estonian Acad. Sci
Sahni, V., Sathyaprakash, B.S., & Shandarin, S.F., 1994, ApJ, 431, 20.
Sahni, V. & Coles, P., 1994, Phys. Rep. in press
Shandarin, S.F., & Zel'dovich, Ya. B., 1989, Rev. Mod. Phys., 61, 185
Vishniac, 1979, MNRAS, 186, 145
Little B., Weinberg D., & Park C., 1991, MNRAS, 253, 295
White, S.D.M., 1979, MNRAS, 186, 145
Zel'dovich, Ya.B., 1970, A&A, 4, 84

Figure 1. The two natural scales of the potential R_* and R_φ (left panel) and the "temperature" γ (right panel) are shown plotted against the spectral index n for featureless power-law spectra. The values of R_* and R_φ are quoted for a box of size 512×512. Note that the difference between the two scales decreases as $|n|$ increases, being largest when $n \simeq 0$ (R_* and R_φ characterize the mean distance between peaks and the correlation length of the potential, respectively.)

Figure 2. Comparison of N-body simulations with the simulations of various approximation schemes. Only a fourth of all the particles are shown. For the sake of clarity, we have superimposed the results of adhesion model over the particle positions of N-body simulations. From top to bottom the pictures correspond to N-body, adhesion model, frozen flow, linear potential, and truncated Zel'dovich approximation, respectively. The left and the right panels are obtained at epochs σ_1 and σ_2, respectively. The plots are shown for (a) $n = 0$, $k_c = 32k_f$, $\sigma_1 = 4$, $\sigma_2 = 16$, (b) $n = 0$, $k_c = 256k_f$, $\sigma_1 = 32$, $\sigma_2 = 128$, (c) $n = 2$, $k_c = 256k_f$, $\sigma_1 = 256$, $\sigma_2 = 1024$,and (d) $n = -2$, $k_c = 256k_f$, $\sigma_1 = 2.00$, $\sigma_2 = 2.83$.

Figure 3. Contour plots of the initial potentials corresponding to the different initial potentials used in our simulations. The solid lines correspond to $\varphi > 0$ and the dashed lines to $\varphi < 0$.

Figure 4. Time evolution of the vector correlation coefficient of particle positions corresponding to (i) frozen flow (dashed line), (ii) linear potential (dotted line), and (iii) truncated Zel'dovich (dashed-dotted line). Top left panel corresponds to $n = 0$, $k_c = 32k_f$ power law model and top right panel to $n = 0$, $k_c = 256k_f$ power law model. Bottom left panel is for $n = 2$, $k_c = 32k_f$ and the one on the bottom right is for $n = -2$, $k_c = 256k_f$. The dotted and the solid vertical lines correspond to the epochs when the scales going nonlinear are R_* and R_φ, respectively.

Figure 5. Evolution of the density correlation coefficient corresponding to (i) adhesion model (solid line), (ii) frozen flow (dashed line), (iii) linear potential (dotted line), and (iv) Zeldovich (dashed-dotted line). In Fig.5a the panels are arranged as in Fig. 4 and before the correlation coefficient is computed the $n = 0$, $k_c = 32k_f$ density field in each simulation is smoothed at $k_G = 16k_f$ and the rest of the density fields are smoothed at $k_G = 64k_f$. In Fig.5b we have shown the evolution of the density correlation coefficient, for the $n = 0$, $k_c = 256k_f$ model, obtained by smoothing the density fields, at a given epcoh, at a scale proportional to the nonlinear scale at that epoch : $k_G^{-1} = 0.5 \times k_{\rm NL}^{-1}$. This demonstrates that while the TZ reproduces the large scale features very accurately, the other approximations, with the exception of the AM, even after such a smoothing, do not show good agreement with N-body results.

Figure 6. Plot showing regions of density greater than the threshold density ρ_c in our N-body simulation for $n = 0$ models. Notice that for the chosen threshold density clumps are well defined features. Top panels correspond to $k_c = 32k_f$ and bottom panels to $k_c = 256k_f$.

Figure 7. Evolution of the number of clumps (top panels) and the total mass in clumps (bottom panels) corresponding to (i) N-body simulations (thick solid line), (ii) adhesion model (solid line), (iii) frozen flow (dashed line), (iv) linear potential (dotted line), and (v) truncated Zel'dovich (dashed-dotted line). The evolution is shown for: (a) $n = 0$ spectrum with left and right panels corresponding, respectively, to, $k_c = 32k_f$ and $k_c = 256k_f$, and (b) for $n = 2$, $k_c = 256k_f$ spectrum (left panels) and $n = -2$, $k_c = 256k_f$ spectrum (right panels).

Figure 8. Filamentary statistic $S(R)$ is shown plotted as a function of the scale length R for two different epochs (as indicated by the value of σ within the panels) corresponding to (i) N-body (thick solid line), (ii) frozen flow (dashed line), (iii) linear potential (dotted line), and (iv) truncated Zel'dovich (dashed-dotted line). Results are shown for (a) $n = 0$ with $k_c = 32k_f$ (top panels), $k_c = 256k_f$ (bottom panels) and (b) $n = 2$, $k_c = 256k_f$ spectrum (top panels) and $n = -2$, $k_c = 256k_f$ spectrum (bottom panels).

Figure 9. Plot showing regions in our N-body simulations of density less than a threshold density ρ_c for $n = 0$ models at two epochs each for cutoff at $k_c = 32k_f$ (top panels) and $k_c = 256k_f$ (bottom panels).

Figure 10. Evolution of the number of voids corresponding to (i) N-body simulations (thick solid line), (ii) adhesion model (solid line), (iii) frozen flow (dashed line), (iv) linear potential (dotted line), and (v) truncated Zel'dovich (dashed-dotted line). The panels are as in Fig. 4.

Figure 11. Void probability function $V(R)$ is shown plotted as a function of the scale R for two different epochs (as indicated by the value of σ within the panels) corresponding to: (i) N-body simulations (thick solid line), (ii) adhesion model (solid line), (iii) frozen flow (dashed line), (iv) linear potential (dotted line), and (v) truncated Zel'dovich (dashed-dotted line). Results are shown for (a) $n = 0$ with $k_c = 32k_f$ (top panel), $k_c = 256k_f$ (bottom panel) and (b) $n = 2$, $k_c = 256k_f$ spectrum (top panel) and $n = -2$, $k_c = 256k_f$ spectrum (bottom panel). The overdensity field needed in finding VPF is determined by taking a threshold density of $\rho_c = 5\rho_0$ in all but $n = 0$, $k_c = 256k_f$ model for which the threshold is taken to be $\rho_c = 2\rho_0$.

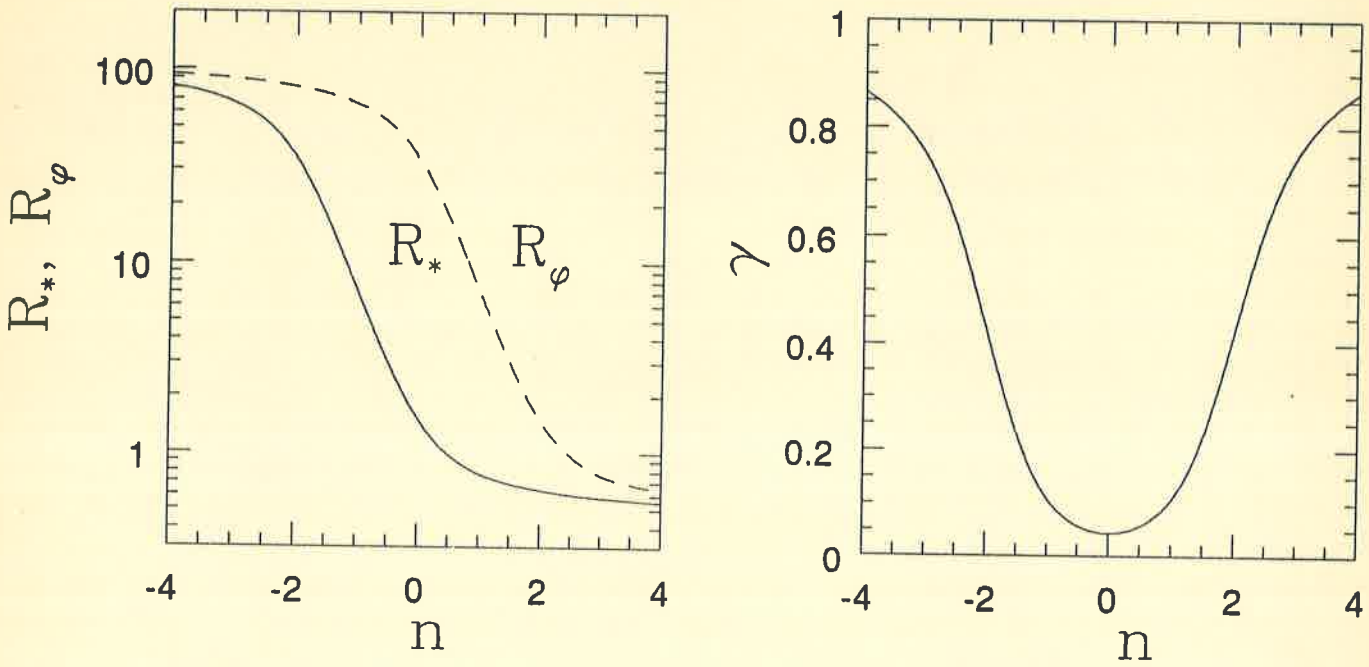

Figure 1

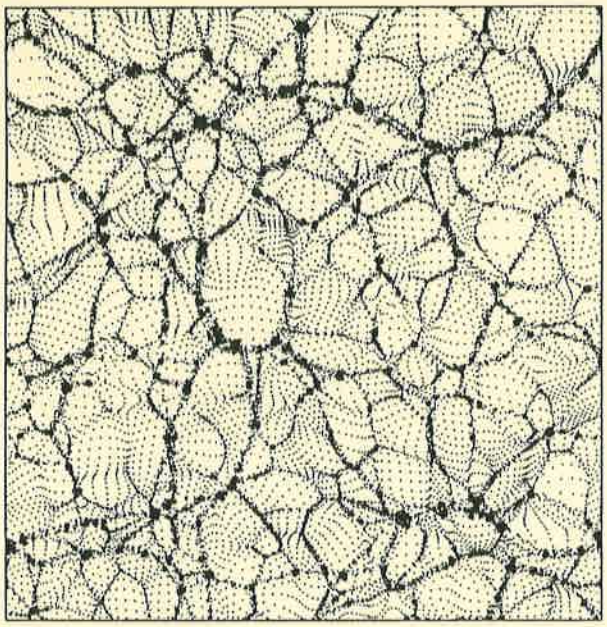

NB

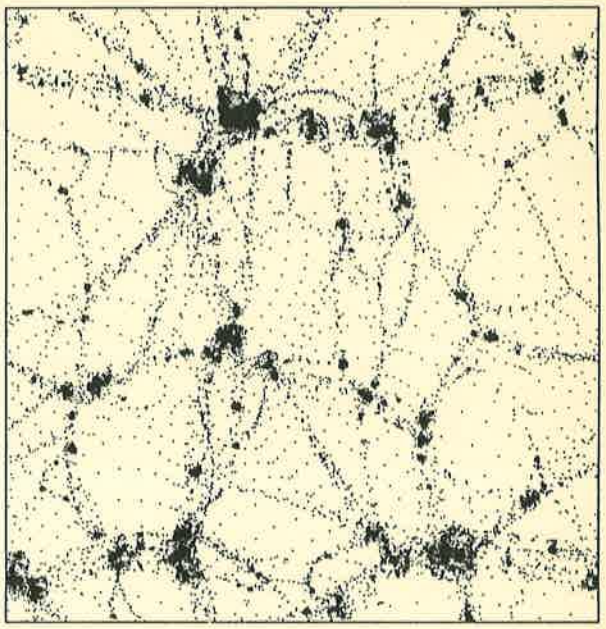

NB

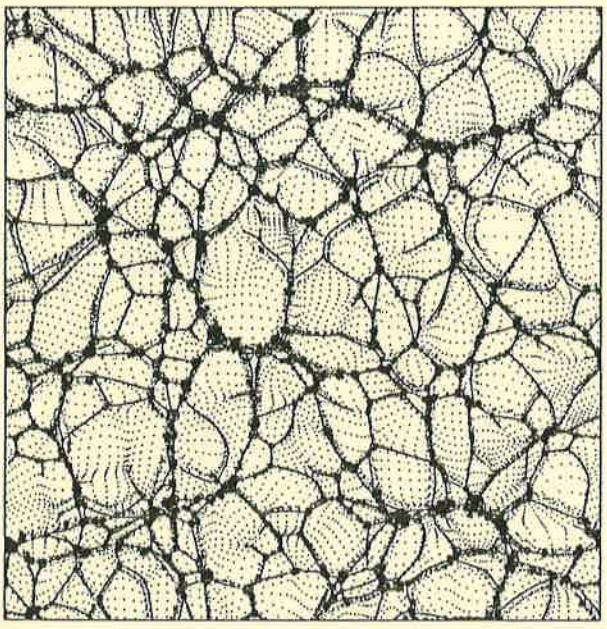

AM

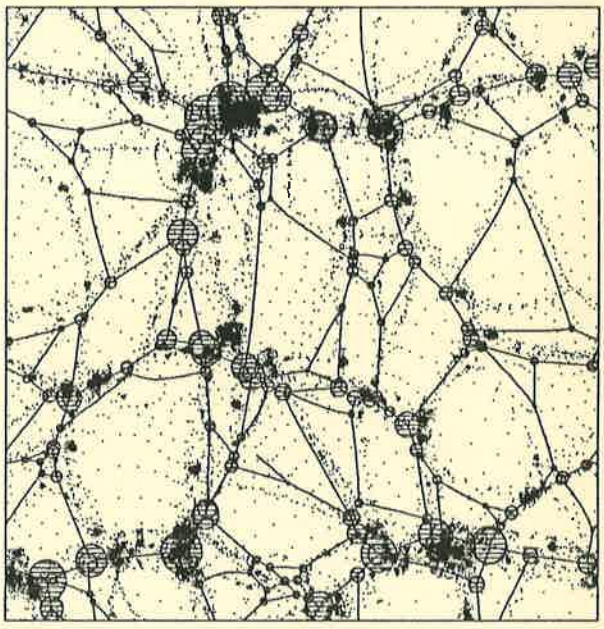

AM

Figure 2a - I

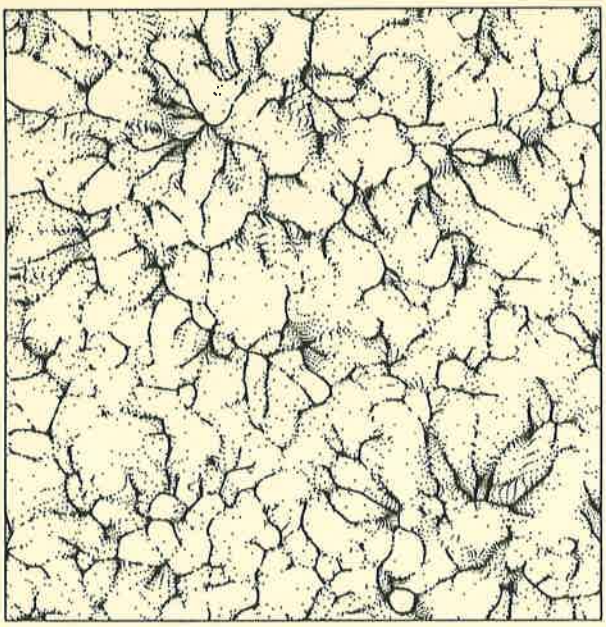

FF

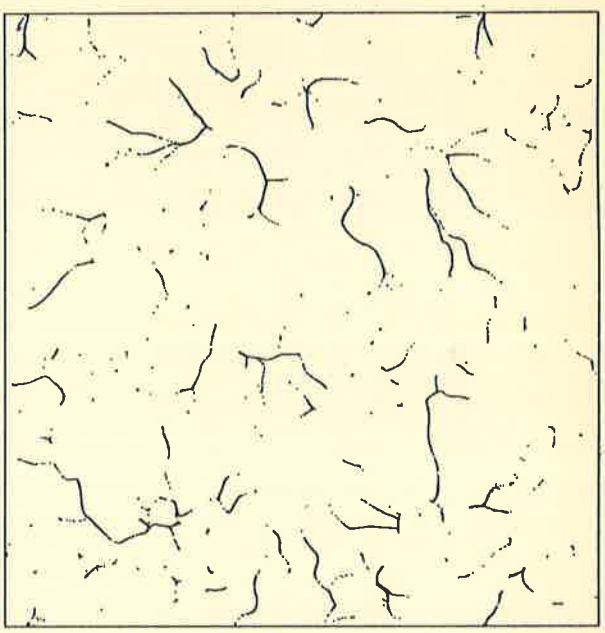

FF

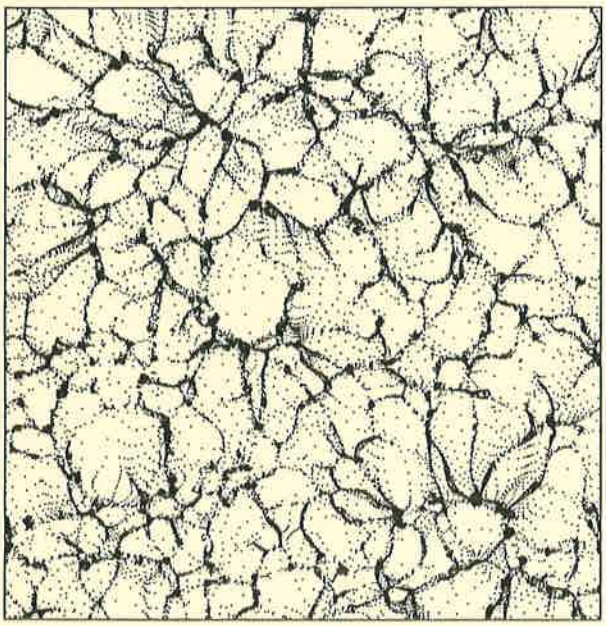

LP

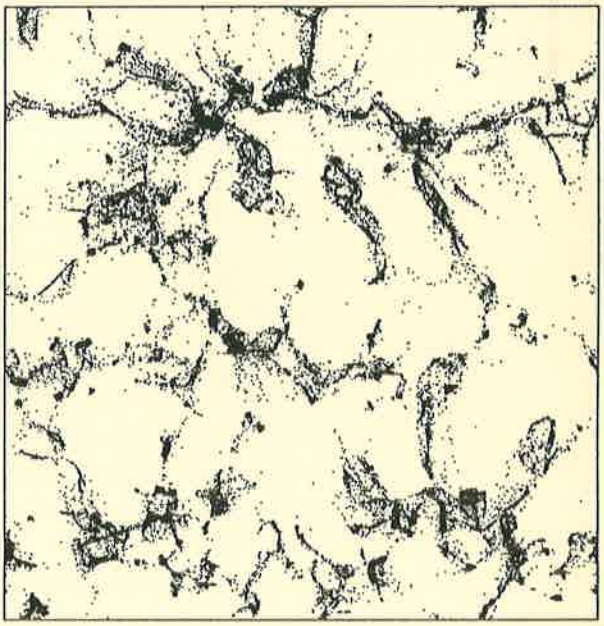

LP

Figure 2a - II

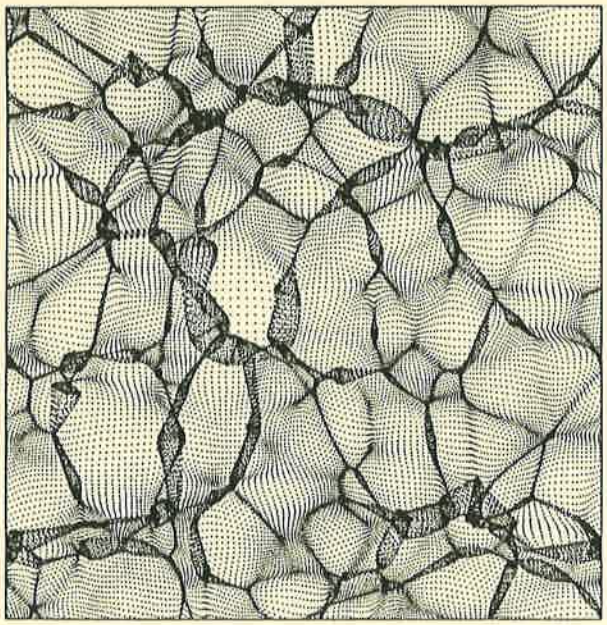

TZ

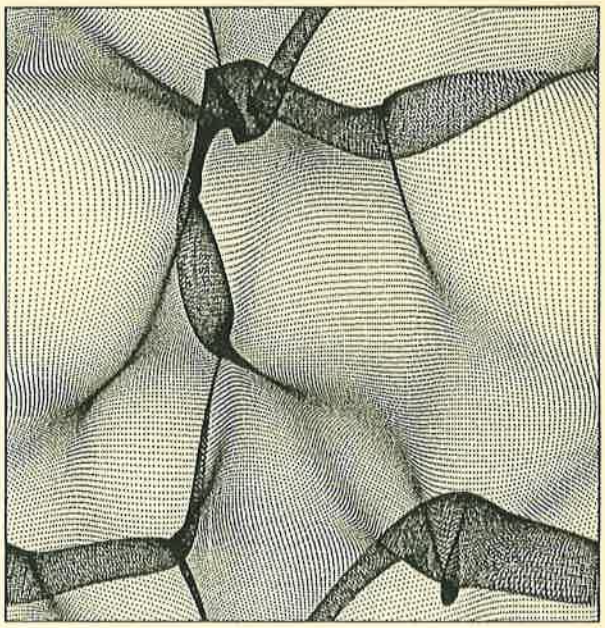

TZ

Figure 2a - III

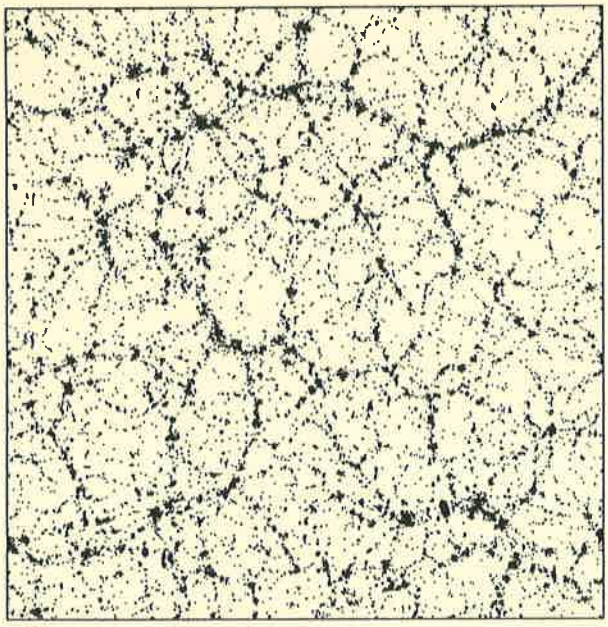

NB

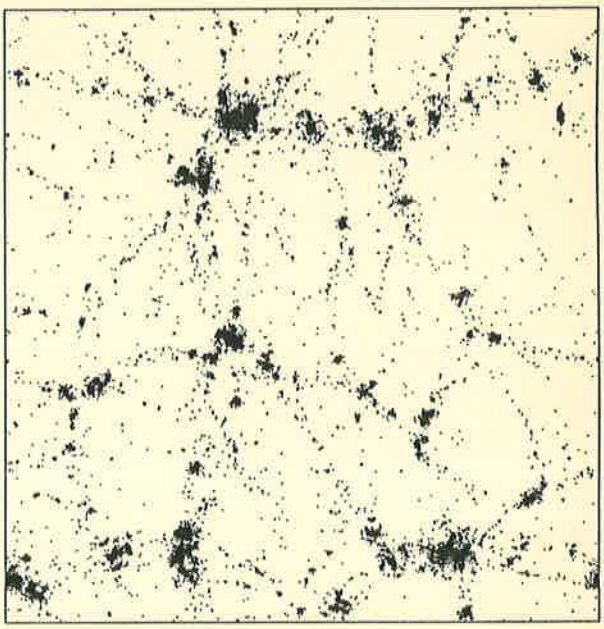

NB

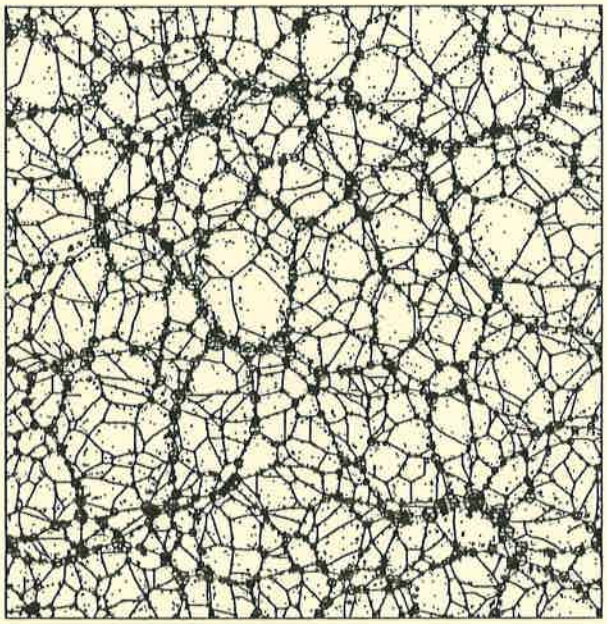

AA

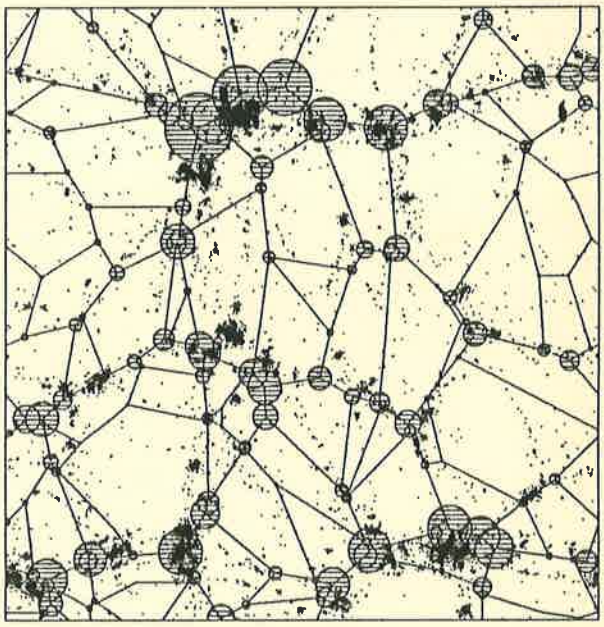

AA

Figure 2b- I

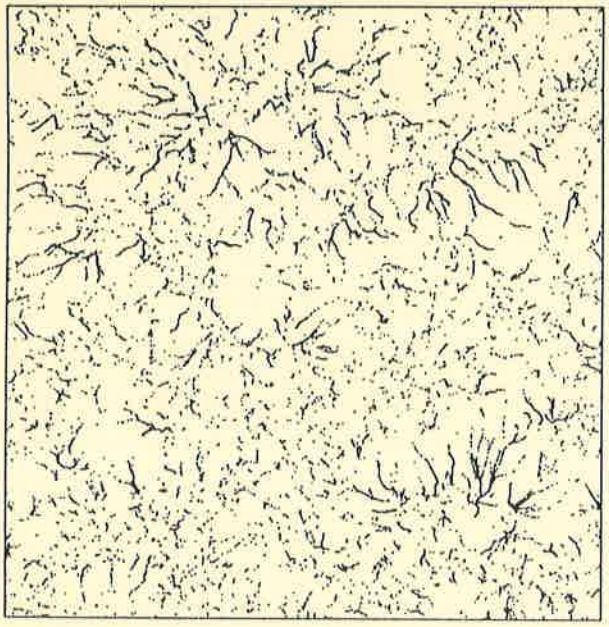

FF

FF

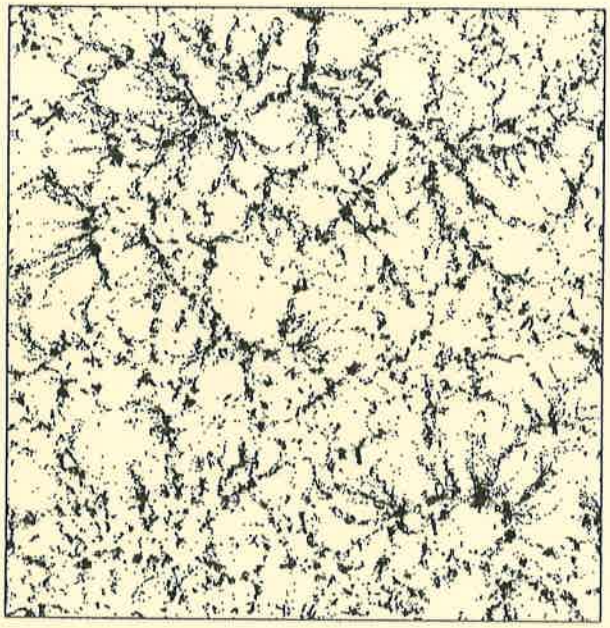

LP

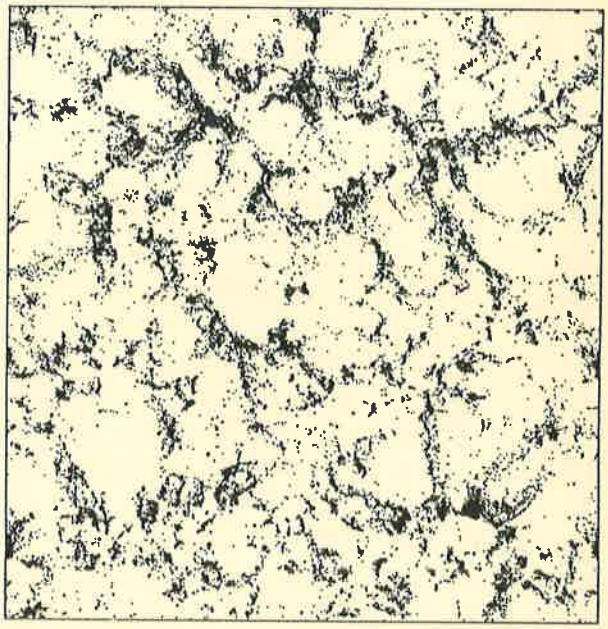

LP

Figure 2b - II

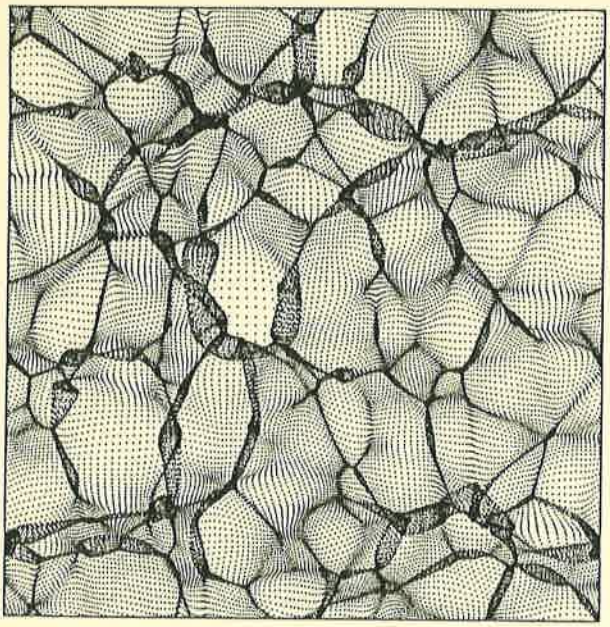

TZ

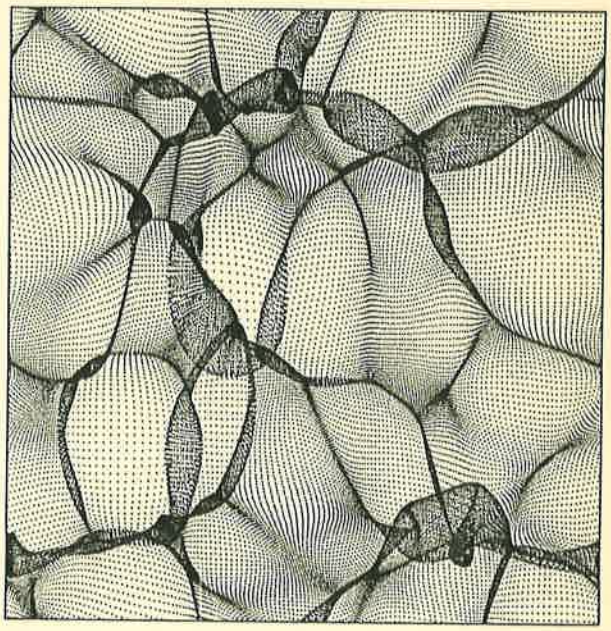

TZ

Figure 2b - III

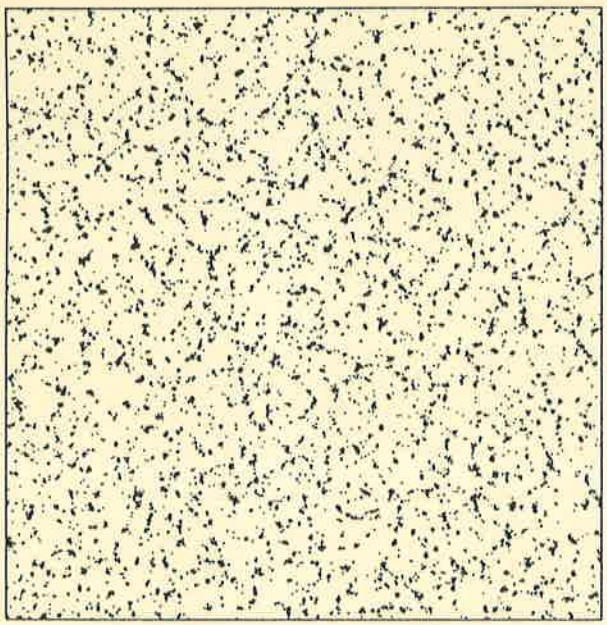

NB

NB

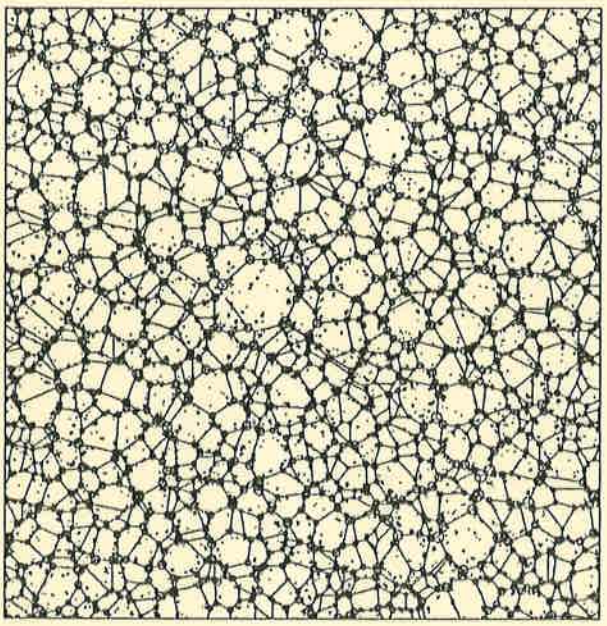

AM

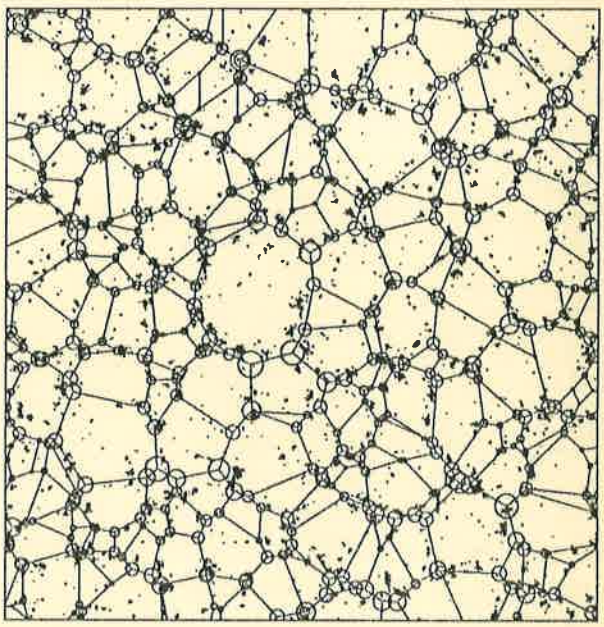

AM

Figure 2c - I

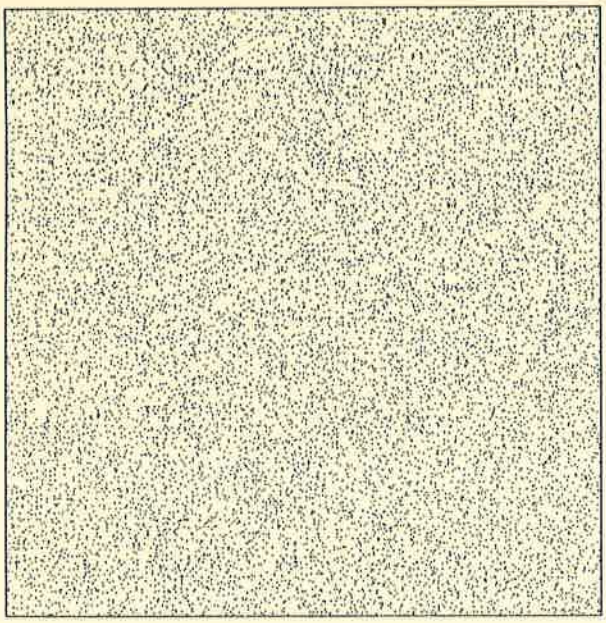

FF

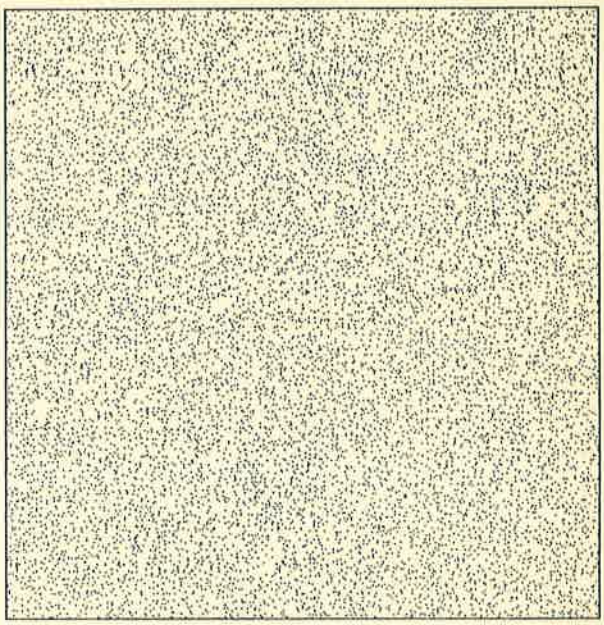

FF

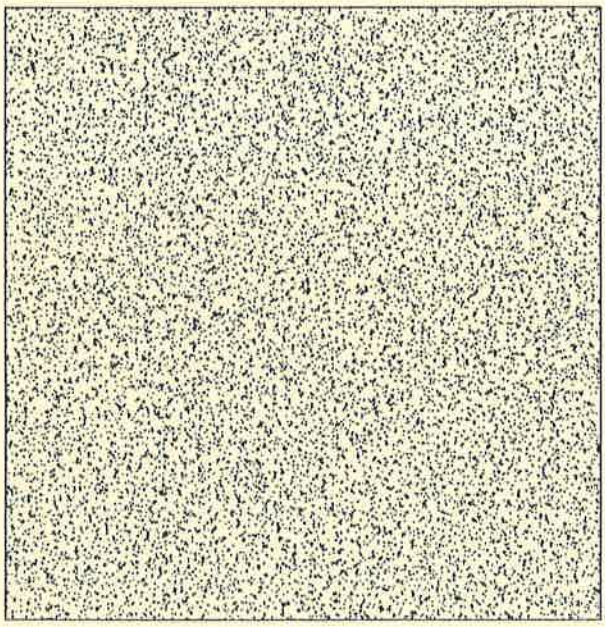

LP

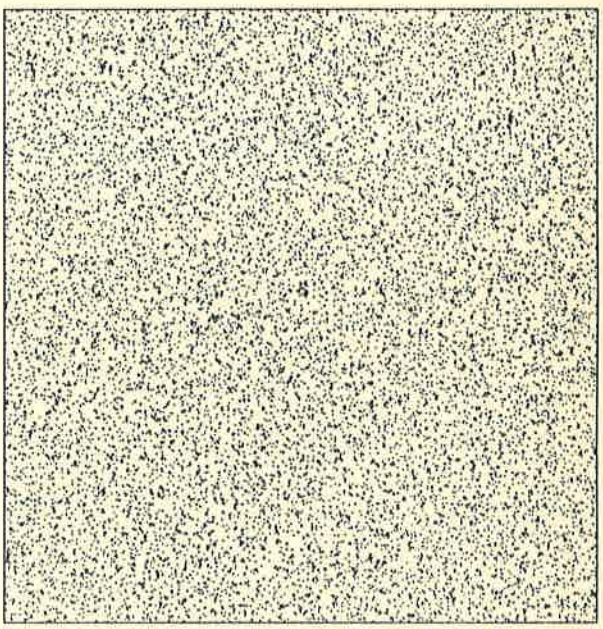

LP

Figure 2c - II

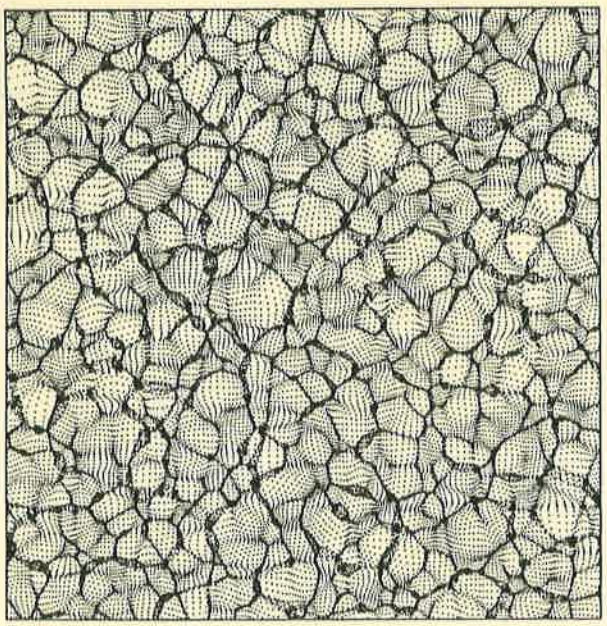

TZ

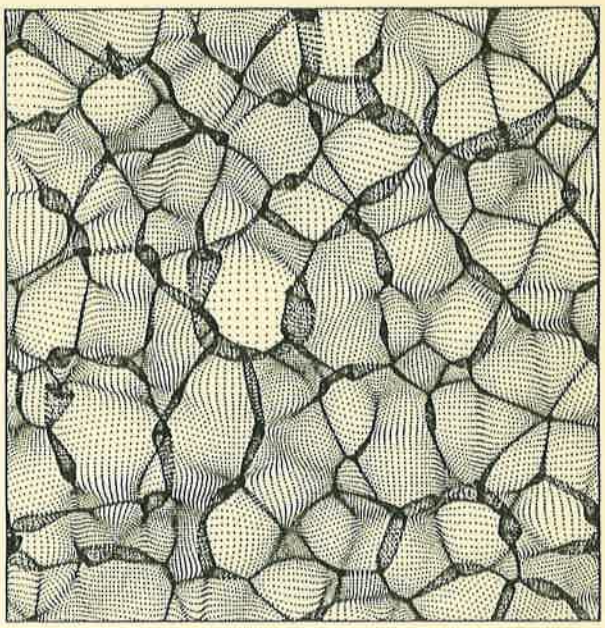

TZ

Figure 2c - III

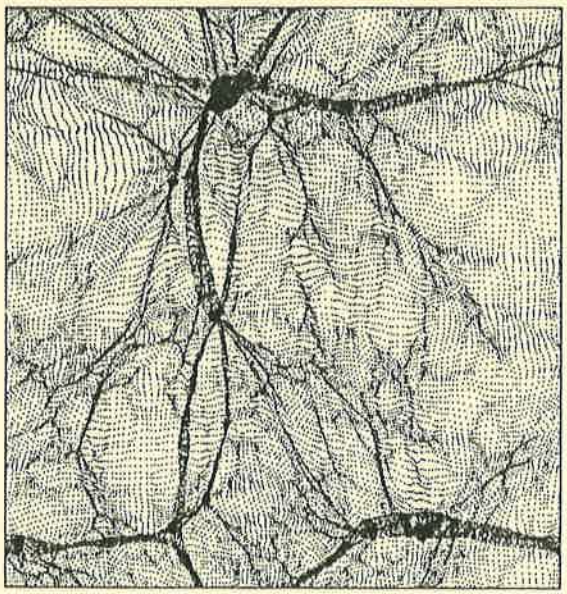

NB

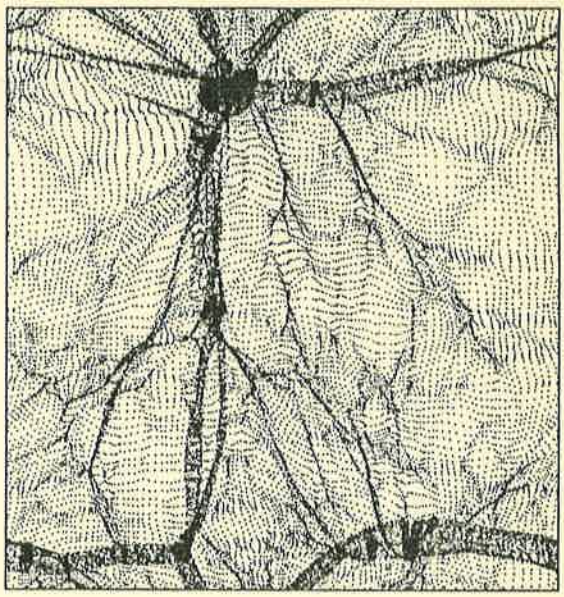

NB

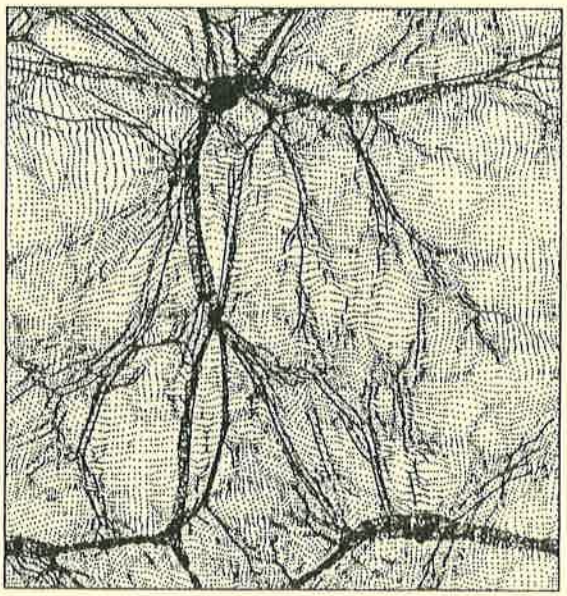

AM

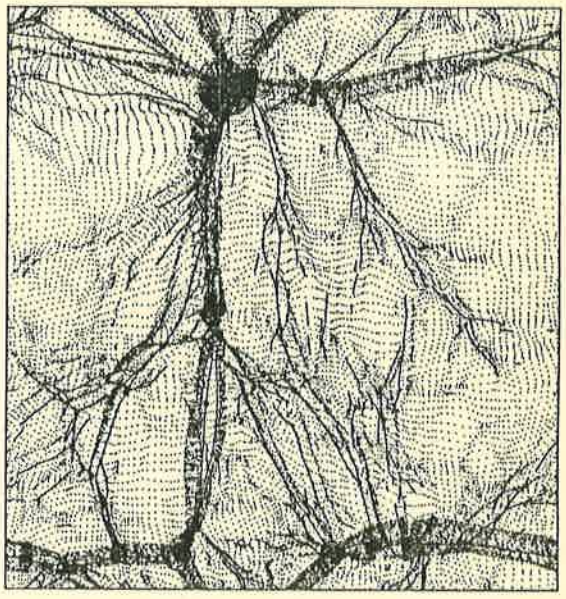

AM

Figure 2d - I

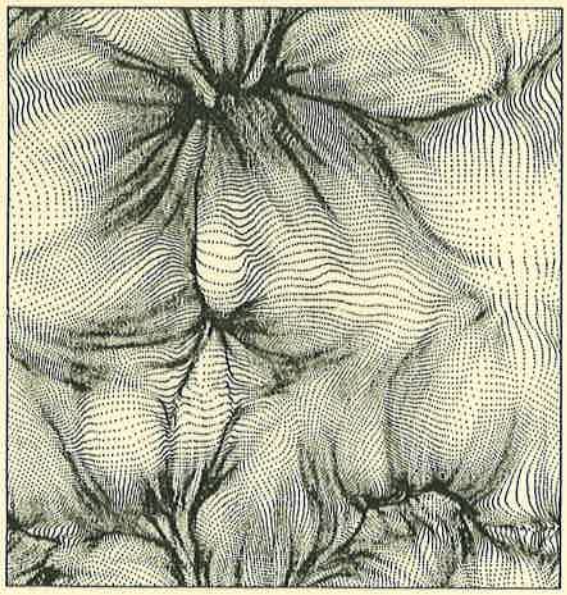

FF

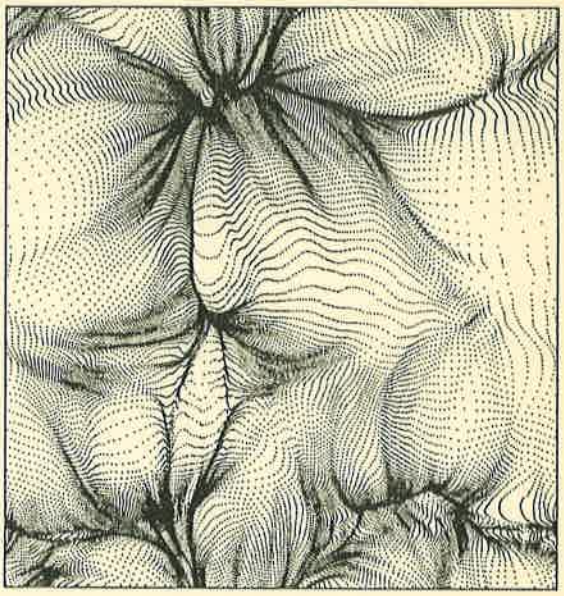

FF

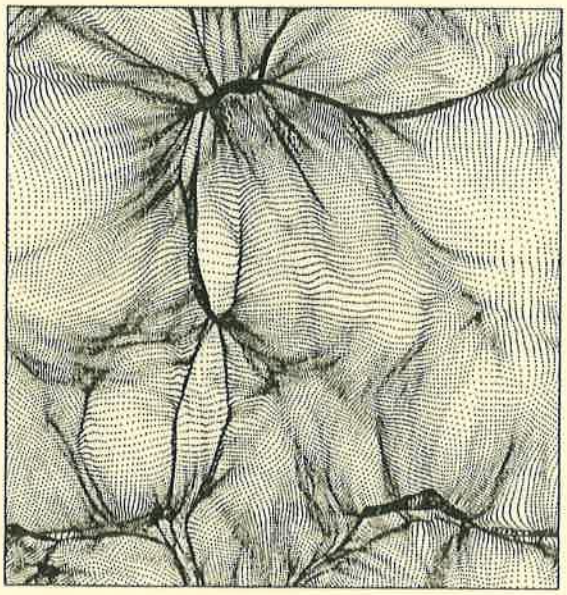

LP

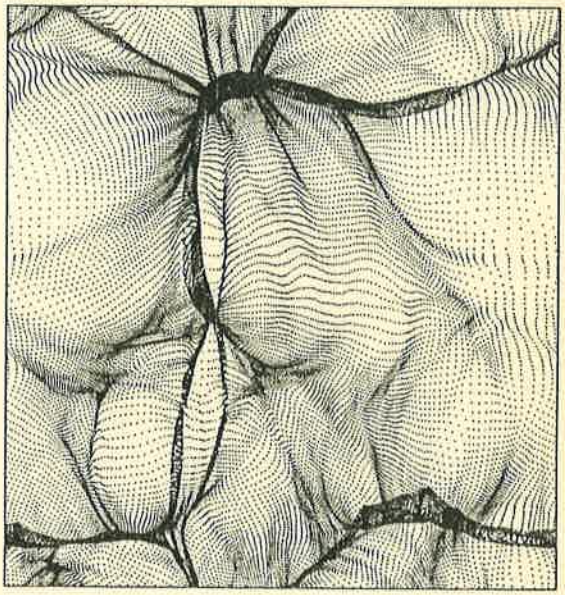

LP

Figure 2d - II

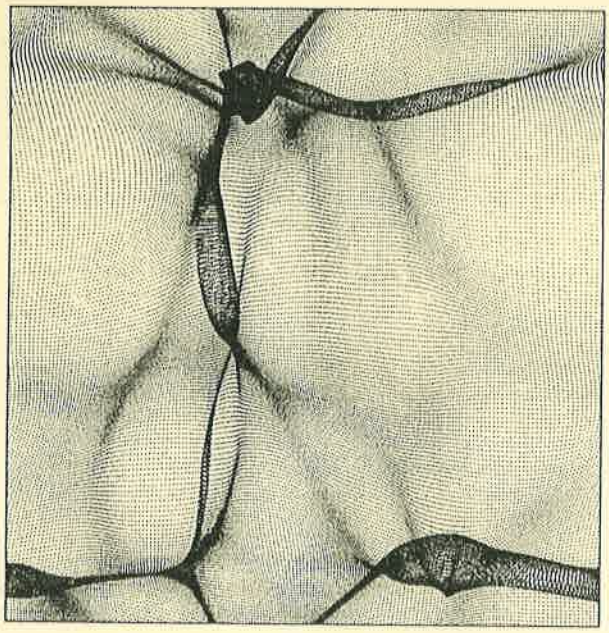

TZ

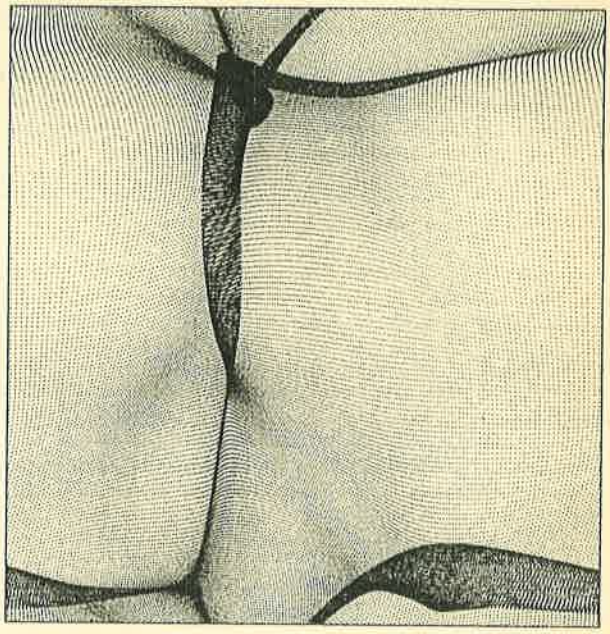

TZ

Figure 2d - III

n=0, Kc=32 Kf

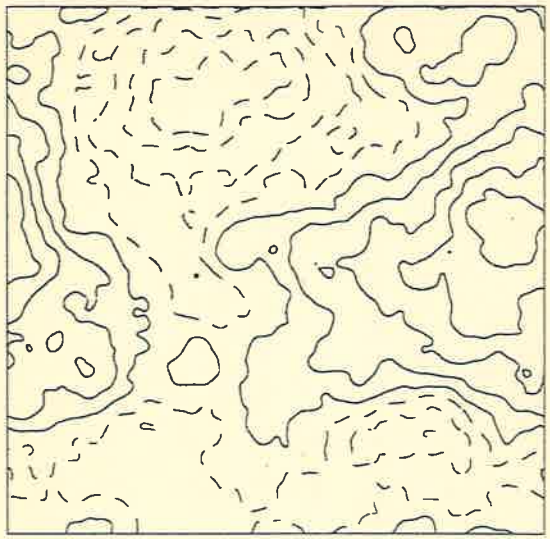

n=0, Kc=256 Kf

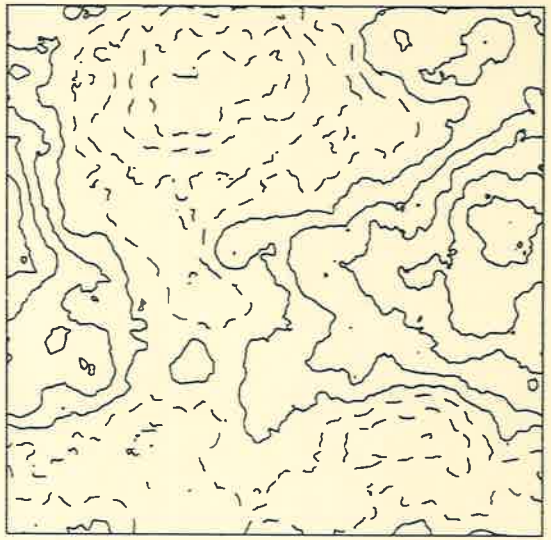

n=2, Kc=256 Kf

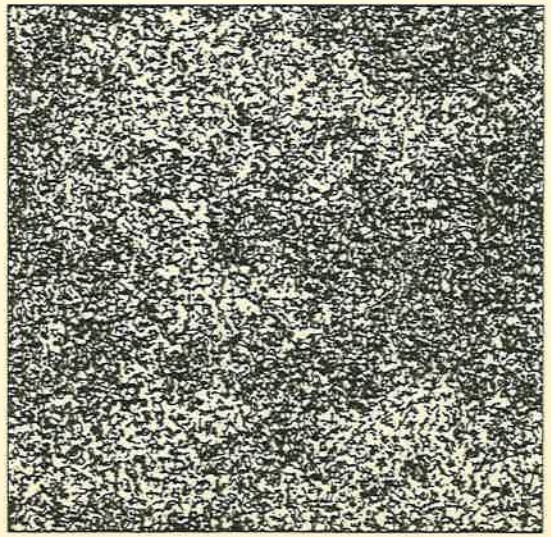

n=−2, Kc=256 Kf

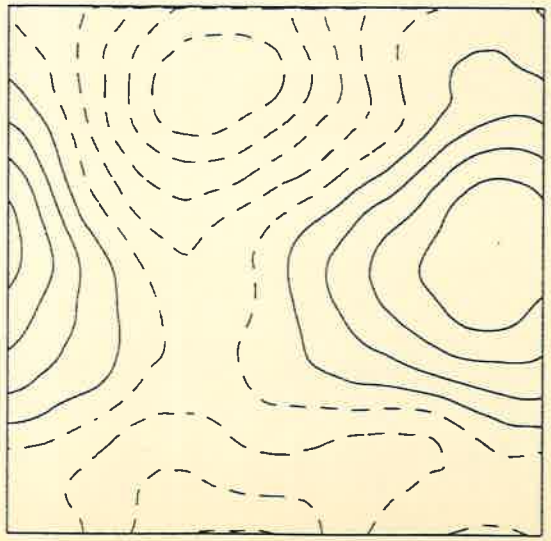

Figure 3

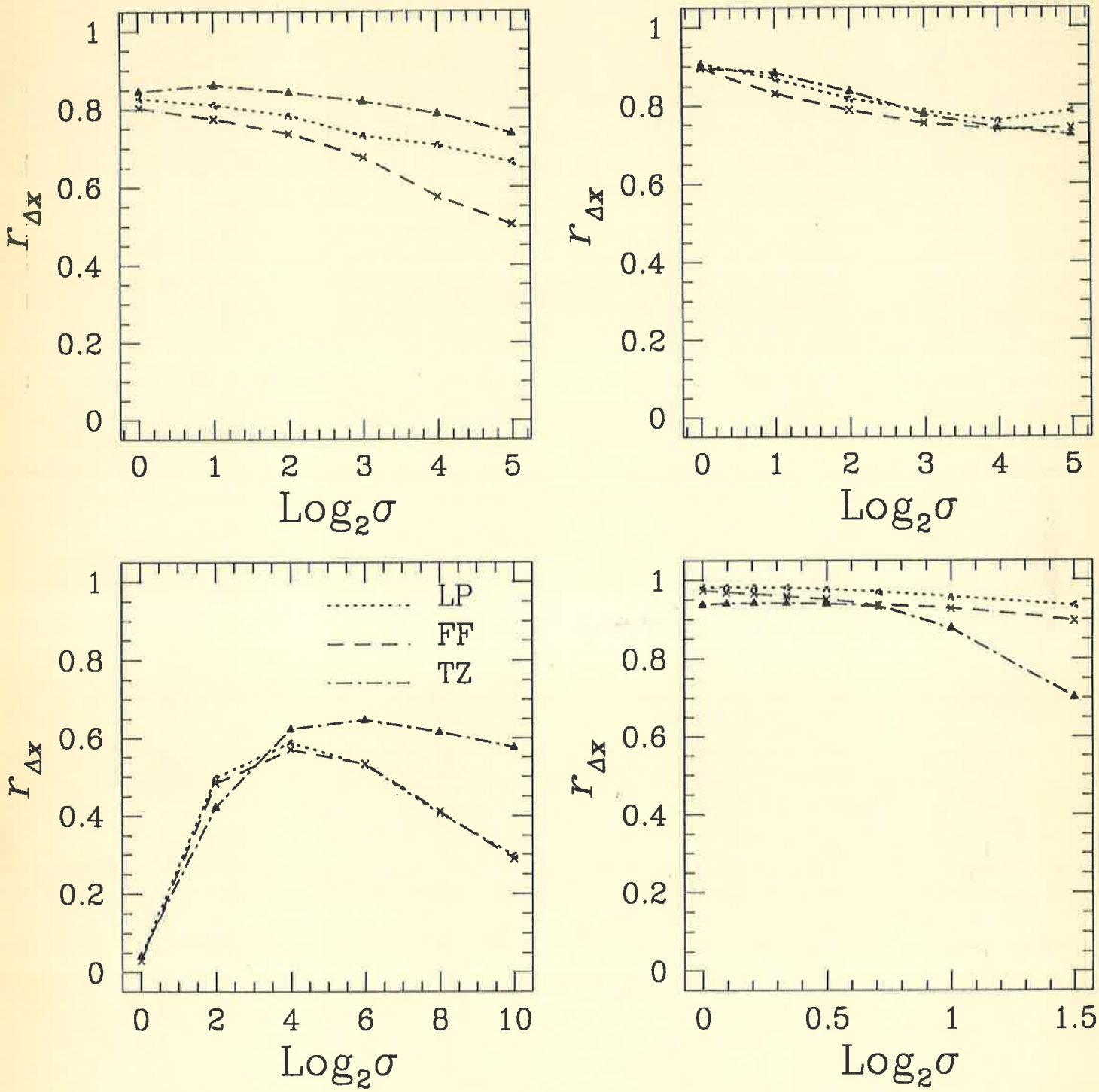

Figure 4

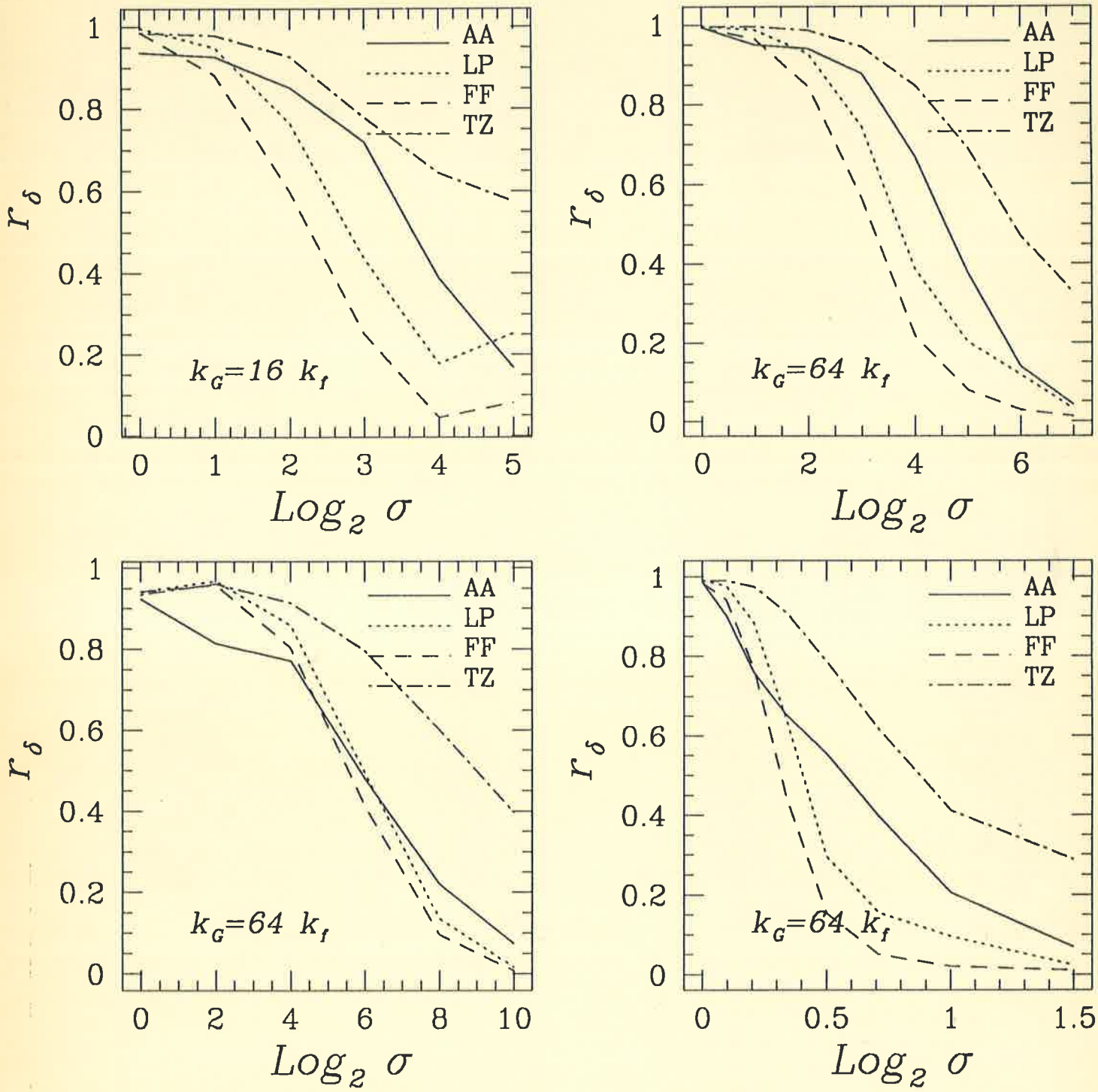
AA
LP
FF
TZ
r_δ
$k_G=16\ k_f$
$k_G=64\ k_f$
$k_G=64\ k_f$
$k_G=64\ k_f$
$Log_2\ \sigma$
$Log_2\ \sigma$
$Log_2\ \sigma$
$Log_2\ \sigma$

Figure 5a

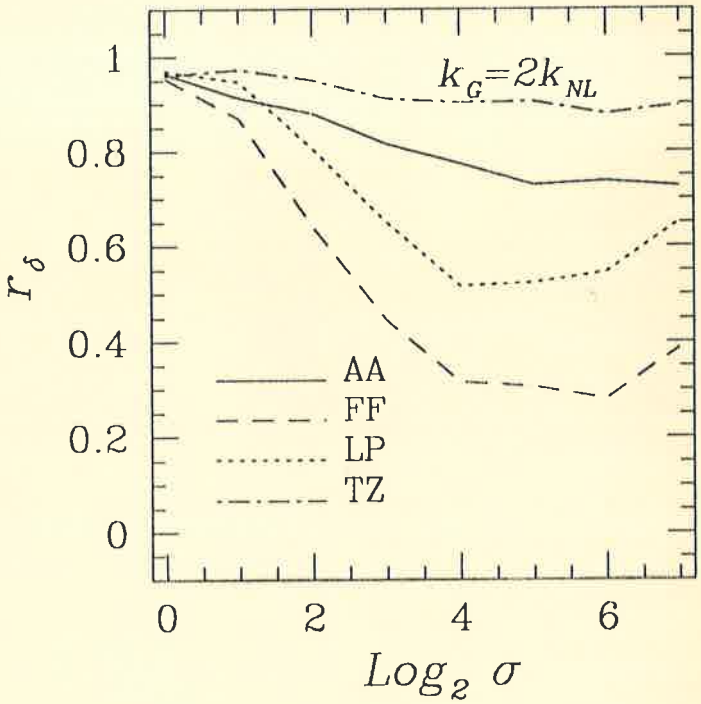

Figure 5b

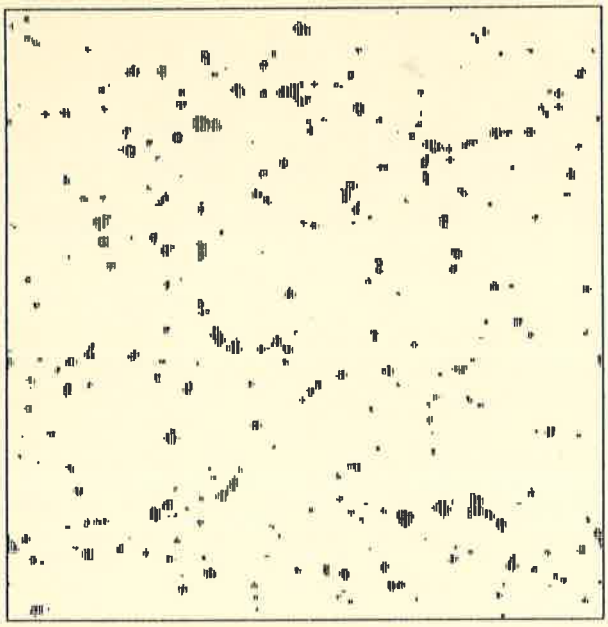

$\sigma=4;\ \rho_c=5\rho_0$

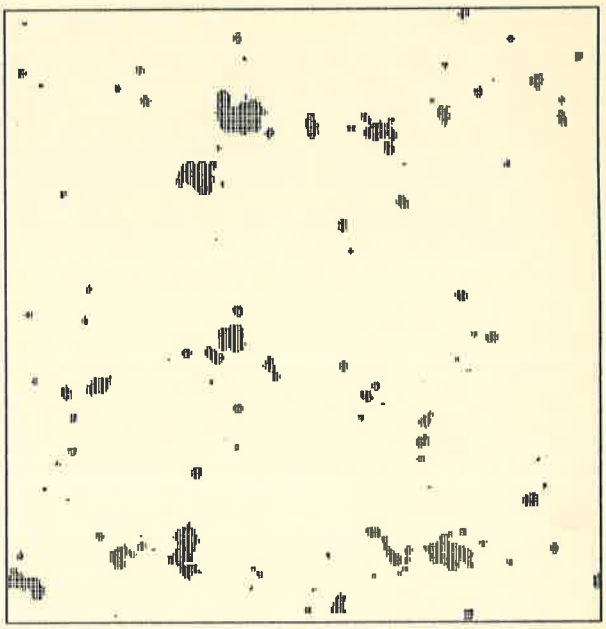

$\sigma=16;\ \rho_c=5\rho_0$

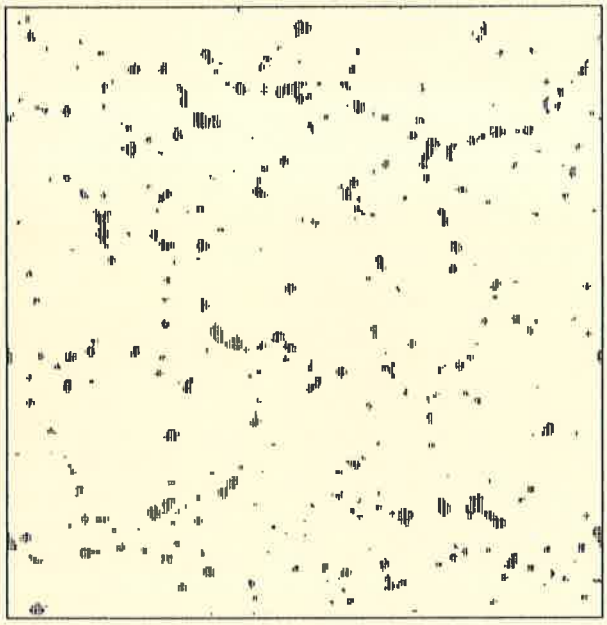

$\sigma=32;\ \rho_c=5\rho_0$

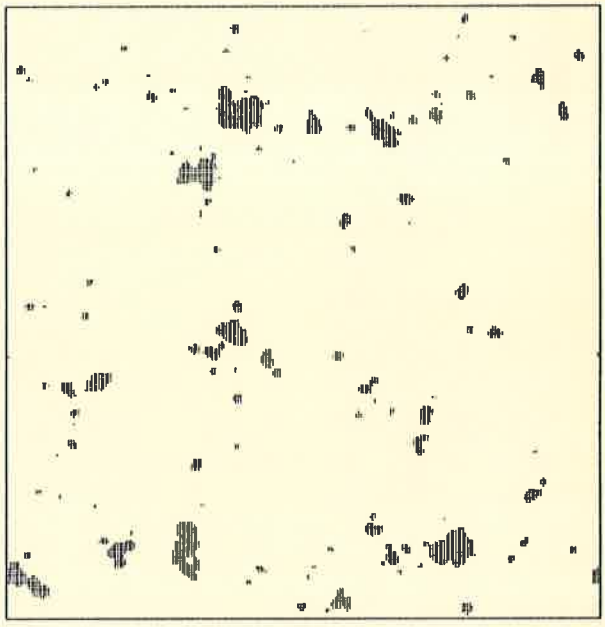

$\sigma=128;\ \rho_c=5\rho_0$

Figure 6

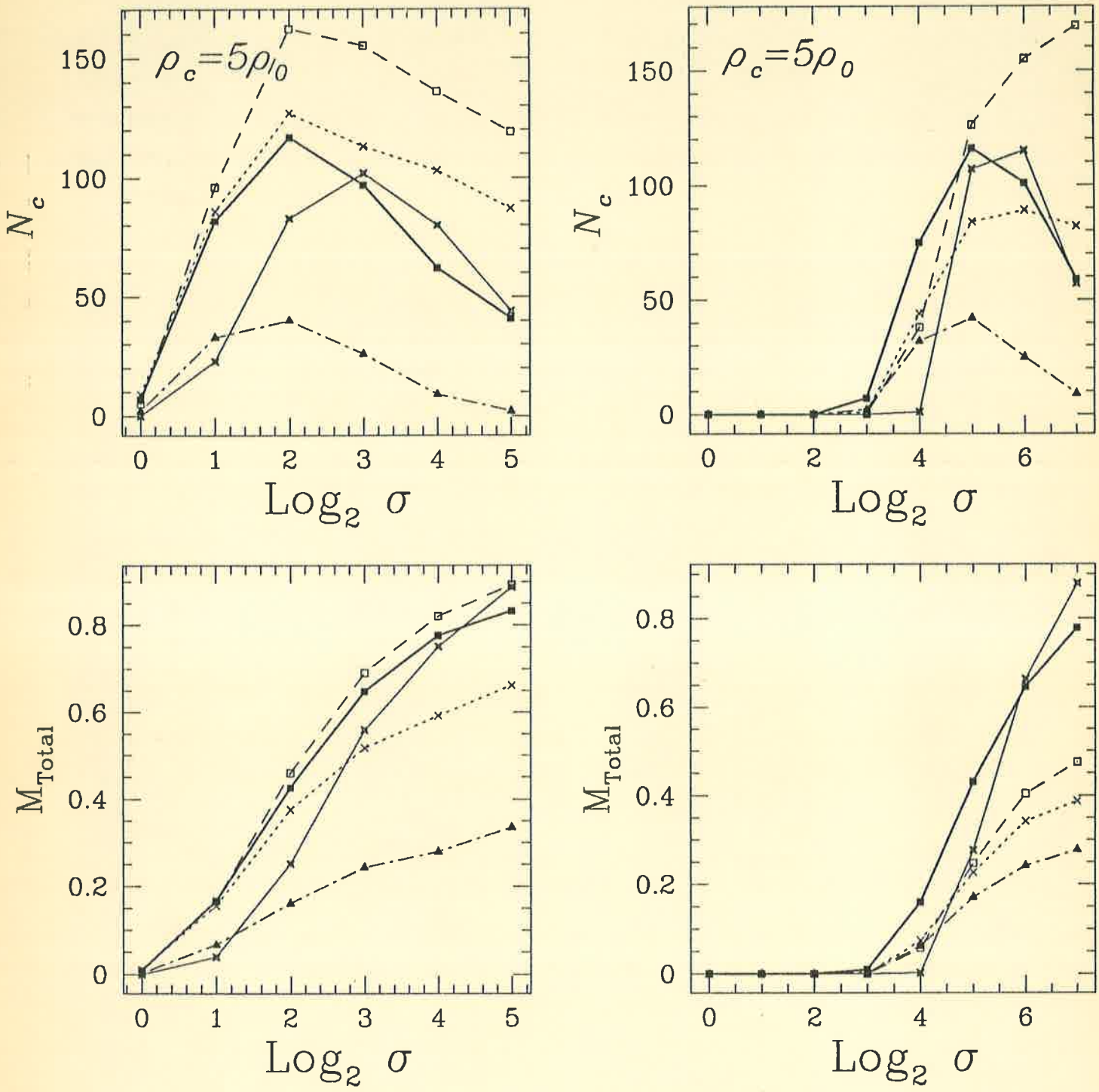
$\rho_c=5\rho_{10}$
$\rho_c=5\rho_0$
N_c
M_{Total}
$Log_2\ \sigma$
0
50
100
150
0.2
0.4
0.6
0.8
1
2
3
4
5
6

Figure 7a

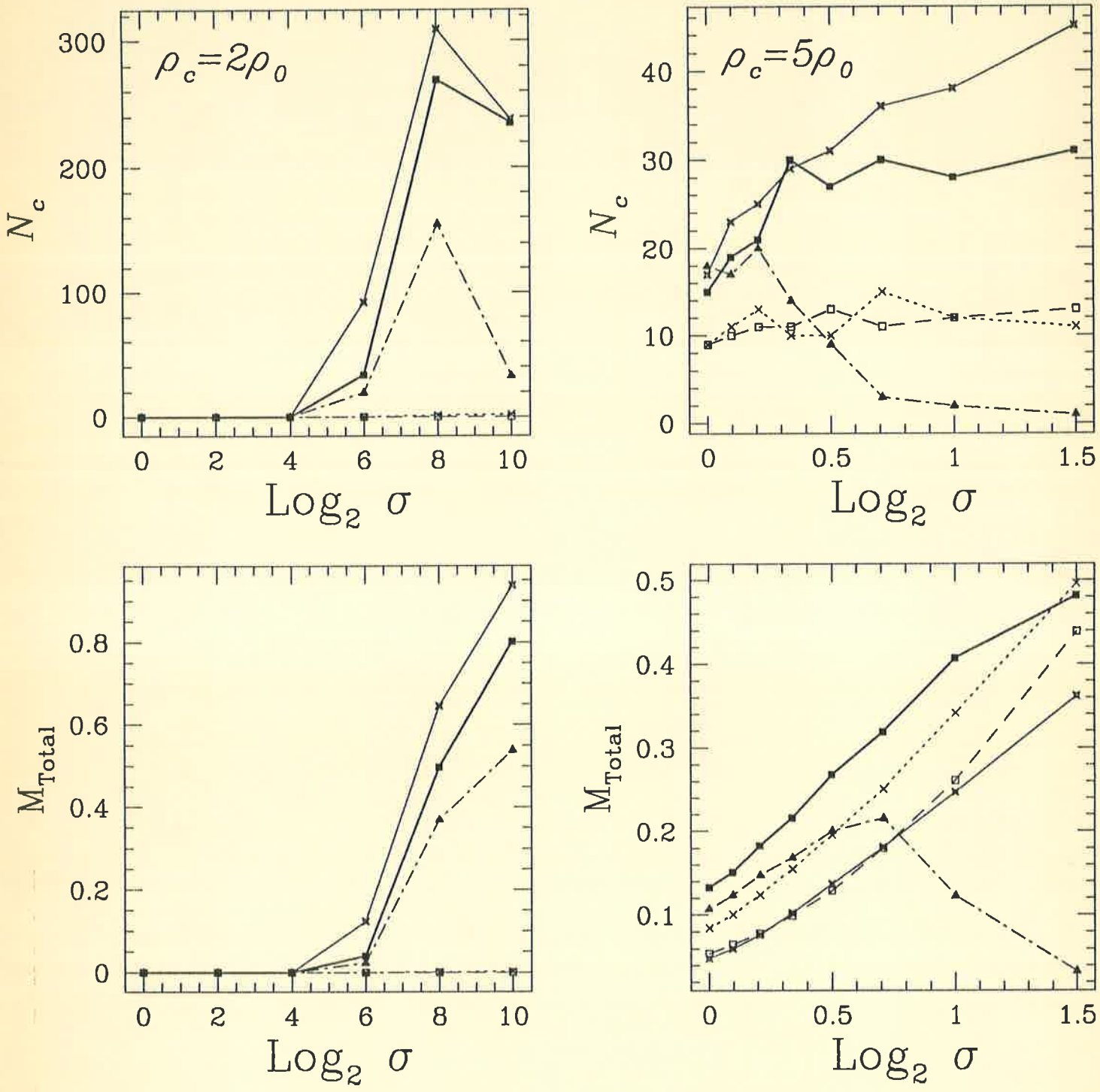
$\rho_c=2\rho_0$
N_c
300
200
100
0
0
2
4
6
8
10
$\mathrm{Log}_2\ \sigma$
$\rho_c=5\rho_0$
N_c
40
30
20
10
0
0
0.5
1
1.5
$\mathrm{Log}_2\ \sigma$
M_{Total}
0.8
0.6
0.4
0.2
0
0
2
4
6
8
10
$\mathrm{Log}_2\ \sigma$
M_{Total}
0.5
0.4
0.3
0.2
0.1
0
0.5
1
1.5
$\mathrm{Log}_2\ \sigma$

Figure 7b

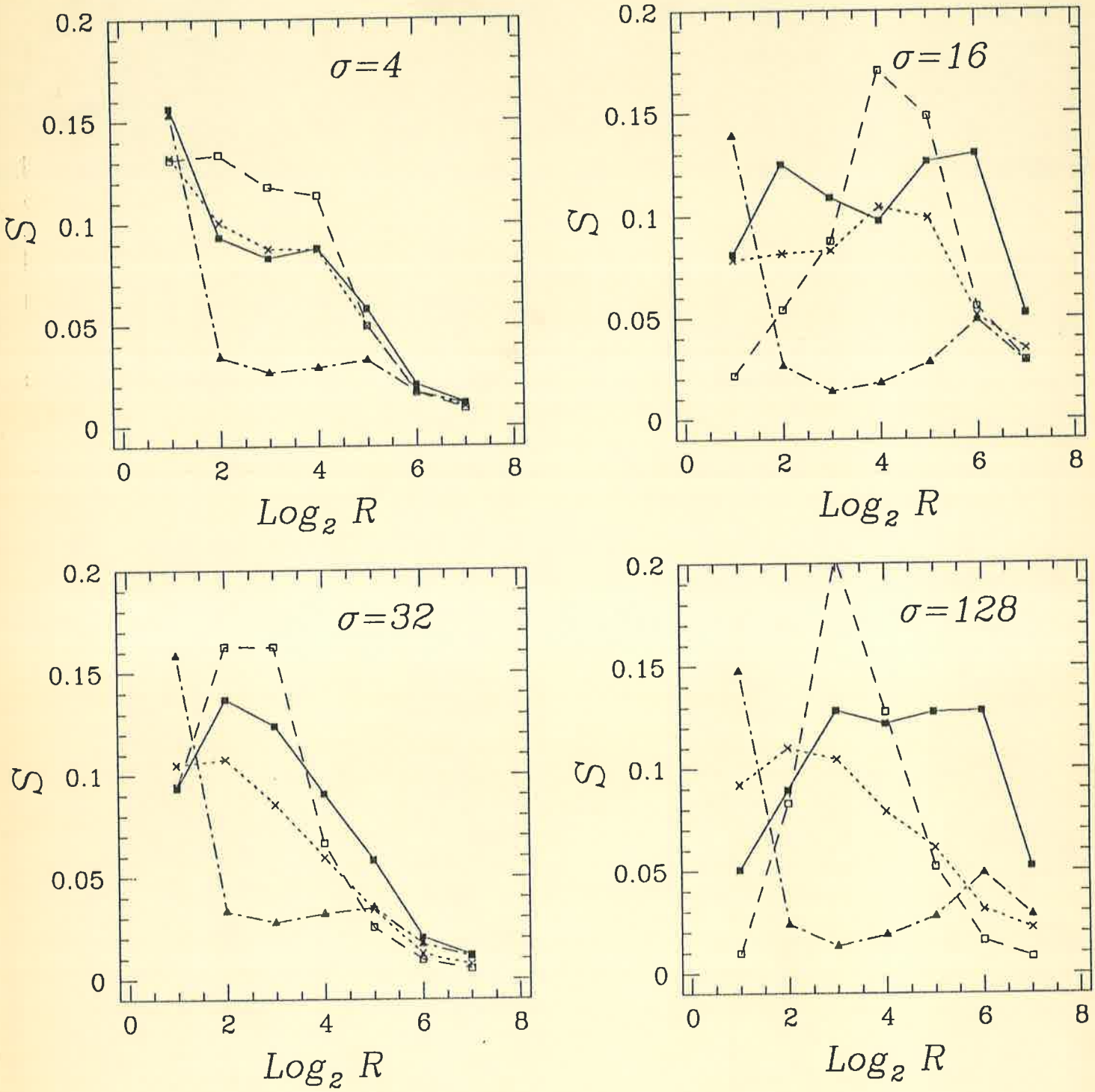

Figure 8a

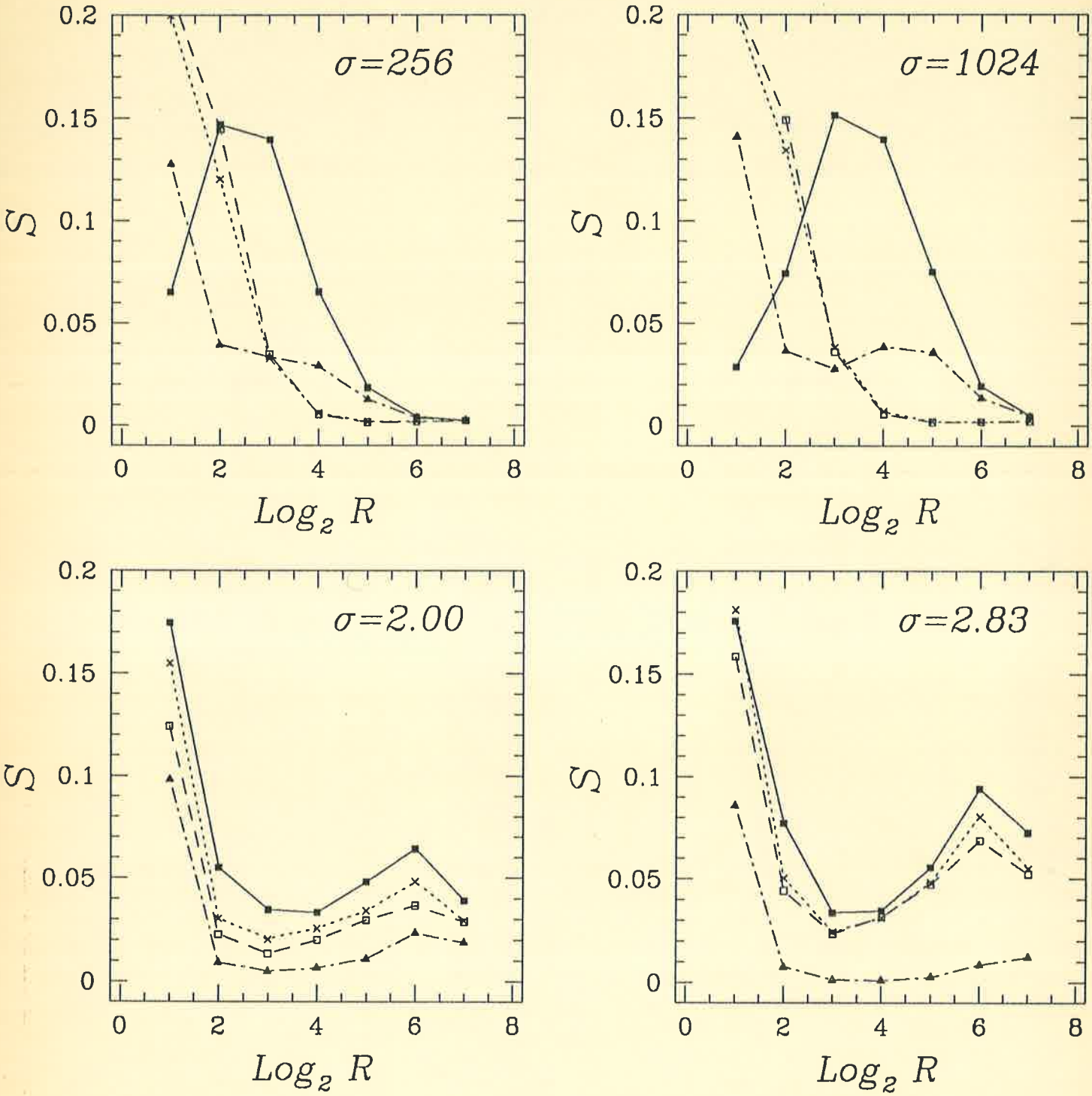

Figure 8b

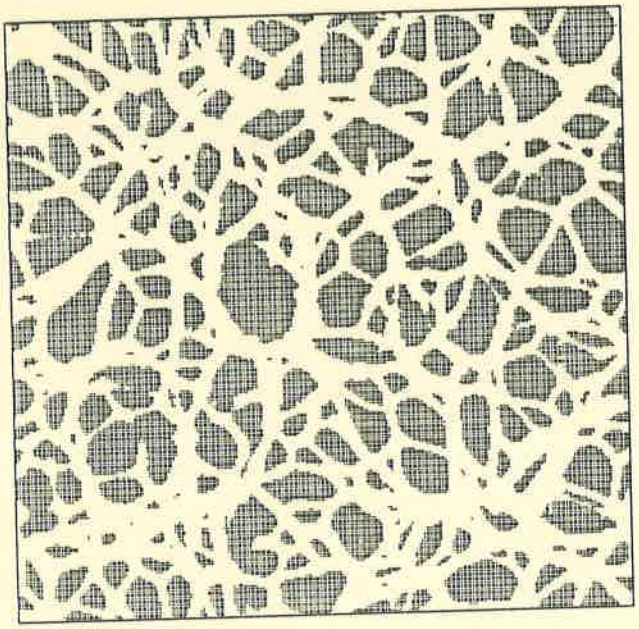

$\sigma=4;\ \rho_c=0.2\rho_0$

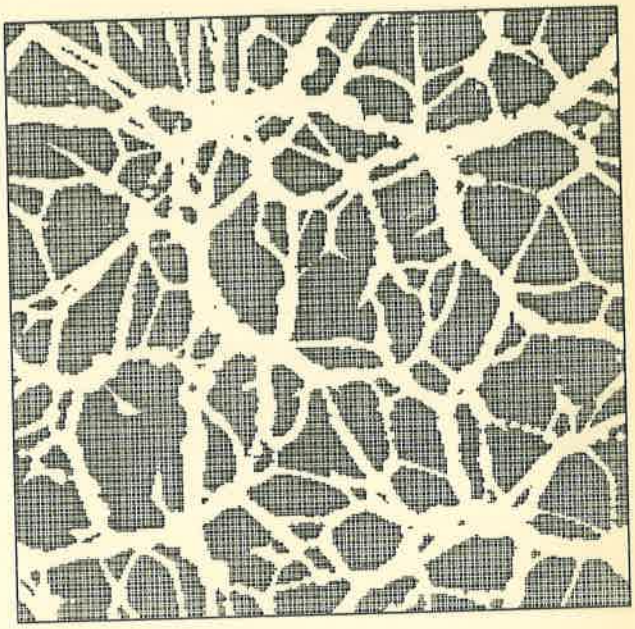

$\sigma=8;\ \rho_c=0.2\rho_0$

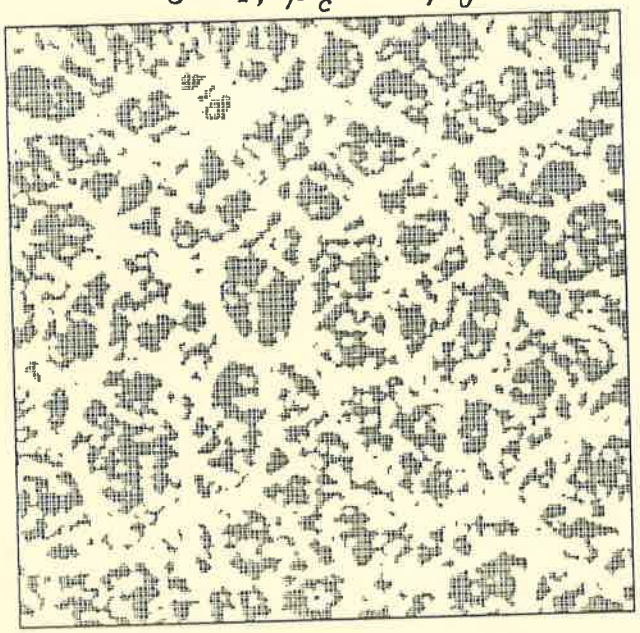

$\sigma=32;\ \rho_c=0.1\rho_0$

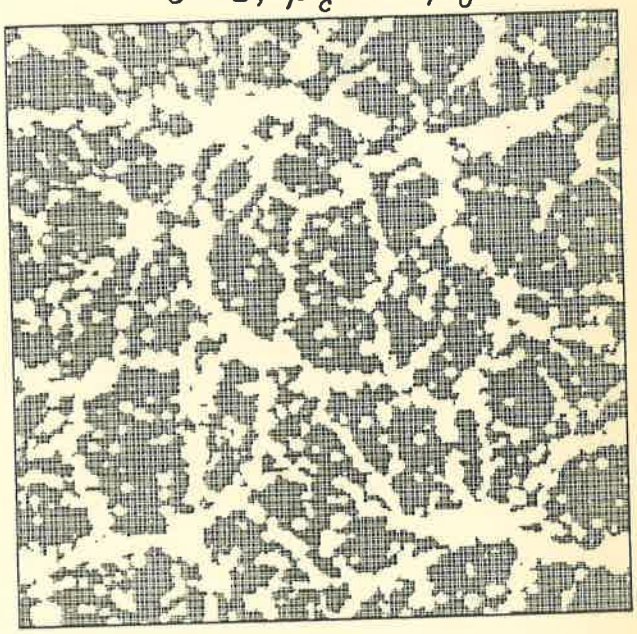

$\sigma=64;\ \rho_c=0.1\rho_0$

Figure 9

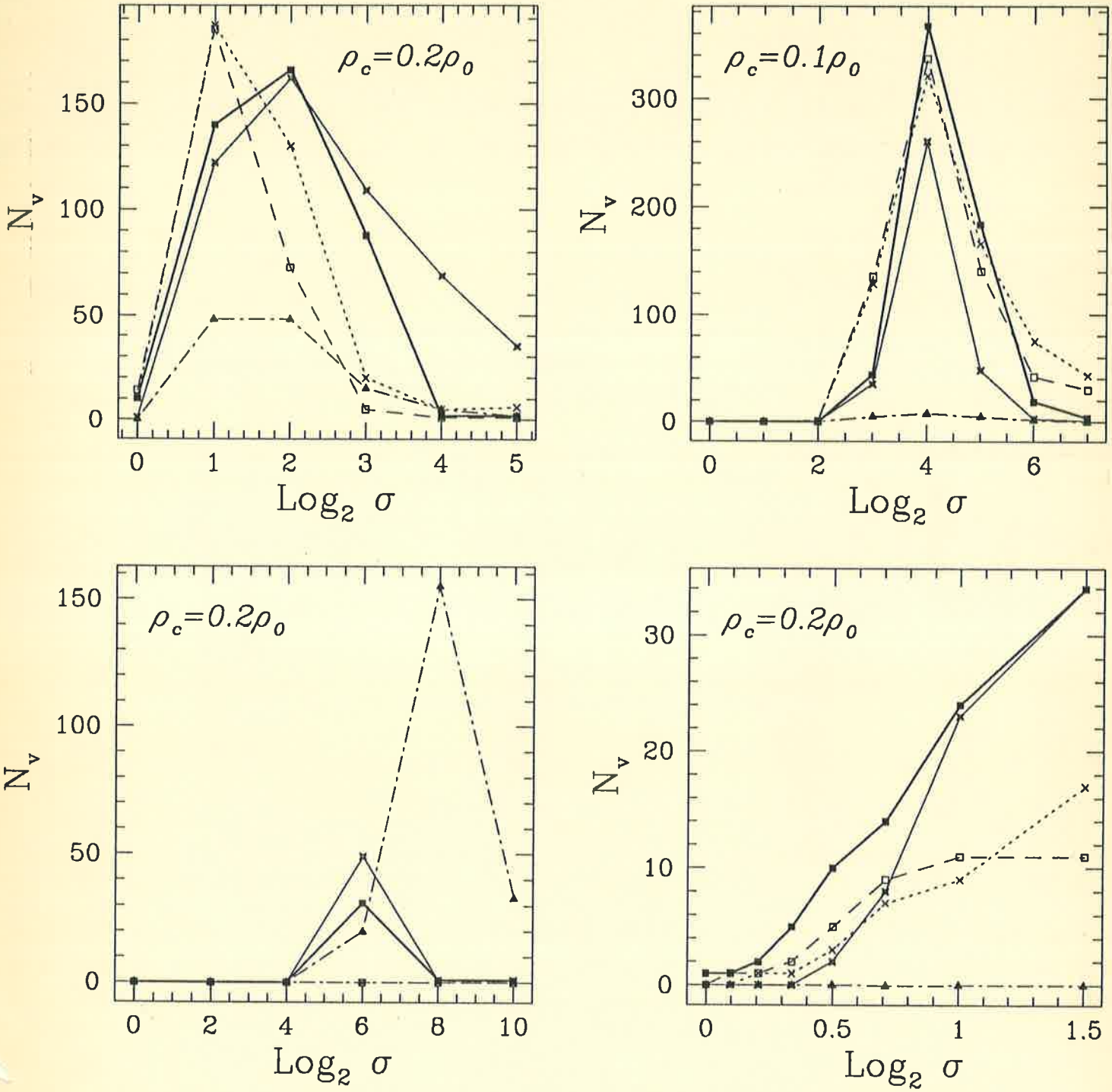
$\rho_c=0.2\rho_0$
$\rho_c=0.1\rho_0$
$\rho_c=0.2\rho_0$
$\rho_c=0.2\rho_0$
N_v
$\mathrm{Log}_2\ \sigma$

Figure 10

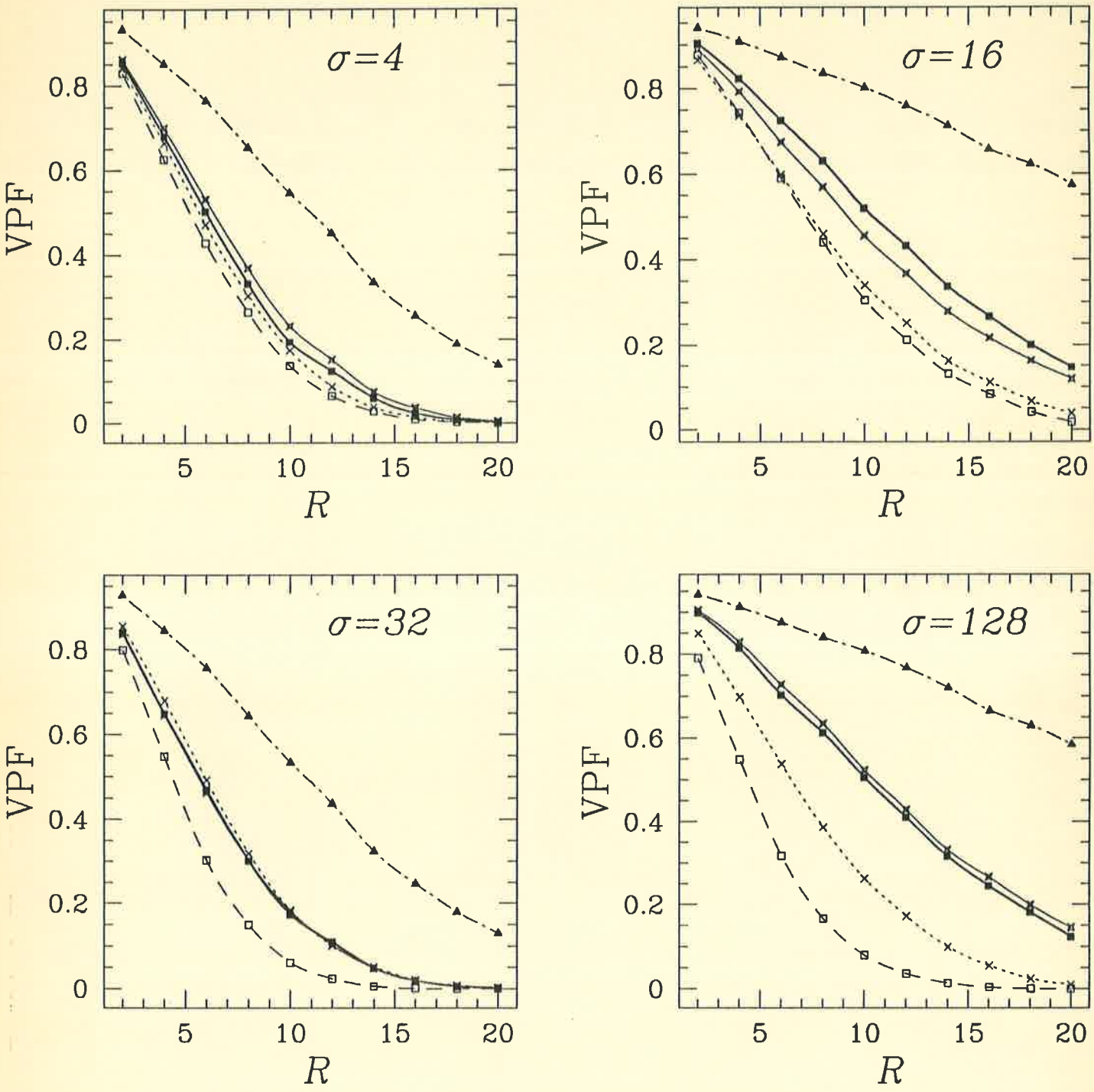

Figure 11a

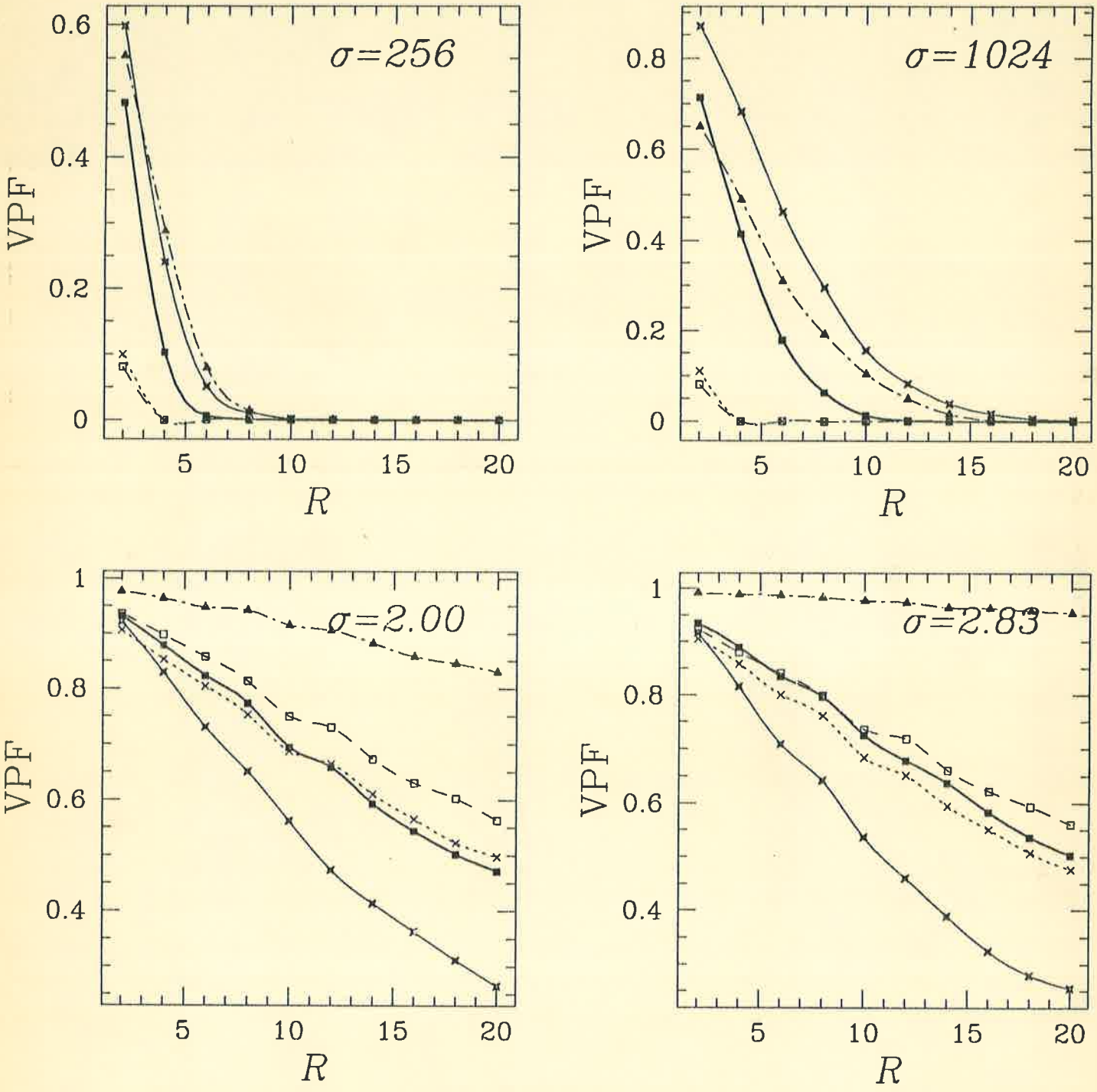

Figure 11b